



1 **A long-term high-resolution air quality reanalysis with public facing air quality dashboard**
2 **over the Contiguous United States (CONUS)**

3

4 Rajesh Kumar¹, Piyush Bhardwaj^{1,*}, Cenlin He¹, Jennifer Boehnert¹, Forrest Lacey¹, Stefano
5 Alessandrini¹, Kevin Sampson¹, Matthew Casali¹, Scott Swerdlin¹, Olga Wilhelmi¹, Gabriele G.
6 Pfister¹, Benjamin Gaubert¹, and Helen Worden¹

7

8 ¹NSF National Center for Atmospheric Research, Boulder, CO, USA

9 *Now at Center for Study of Science, Technology and Policy (CSTEP), Bengaluru, India

10

11 Corresponding author: Rajesh Kumar (rkumar@ucar.edu)

12

13 Keywords: Chemical data assimilation, WRF-CMAQ, GSI, Air Quality Dashboard

14

15

16



17 **Abstract**

18 We present a 14-year 12-km hourly air quality dataset created by assimilating satellite observations
19 of aerosol optical depth (AOD) and carbon monoxide (CO) in an air quality model to fill gaps in
20 the contiguous United States (CONUS) air quality monitoring network and help air quality
21 managers understand long-term changes in county level air quality. Specifically, we assimilate the
22 Moderate Resolution Imaging Spectroradiometer (MODIS) AOD and the Measurement of
23 Pollution in the Troposphere (MOPITT) CO observations in the Community Multiscale Air
24 Quality Model (CMAQ) every day from 01 Jan 2005 to 31 Dec 2018 to produce this dataset. The
25 Weather Research and Forecasting (WRF) model simulated meteorological fields are used to drive
26 CMAQ offline and to generate meteorology dependent anthropogenic emissions. Both the weather
27 and air quality (surface fine particulate matter (PM_{2.5}) and ozone) simulations are subjected to a
28 comprehensive evaluation against multi-platform observations to establish the credibility of our
29 dataset and characterize its uncertainties. We show that our dataset captures regional hourly,
30 seasonal, and interannual variability in meteorology very well across the CONUS. The correlation
31 coefficient between the observed and simulated surface ozone and PM_{2.5} concentrations for
32 different Environmental Protection Agency (EPA) defined regions across CONUS are 0.77-0.91
33 and 0.49-0.79, respectively. The mean bias and root mean squared error for modeled ozone are
34 3.7-6.8 ppbv and 7-9 ppbv, respectively, while the corresponding values for PM_{2.5} are -0.9-5.6
35 $\mu\text{g}/\text{m}^3$ and 3.0-8.3 $\mu\text{g}/\text{m}^3$, respectively. We estimate that annual CONUS averaged maximum daily
36 8-hour average (MDA8) ozone and PM_{2.5} trends are -0.30 ppb/year and -0.24 $\mu\text{g}/\text{m}^3/\text{year}$,
37 respectively. Wintertime MDA8 ozone shows an increasing but statistically insignificant trend at
38 several sites. We also found a decreasing trend in the 95th percentile of MDA8 ozone but an
39 increasing trend in the 5th percentile. Most of the sites in the Pacific Northwest show an increasing



40 but statistically insignificant trend during summer. An ArcGIS air quality dashboard has been
41 developed to enable easy visualization and interpretation of county level air quality measures and
42 trends by stakeholders, and a Python-based Streamlit application has been developed to allow the
43 download of the air quality data in simplified text and graphic formats.

44

45



46 1. Introduction

47 Air quality is one of the most important global environmental concerns as almost the entire global
48 population (99%) is estimated to breathe air that exceeds the World Health Organization (WHO)
49 defined Air Quality Guidelines (WHO, 2023). Exposure to ambient air pollution causes about 4.2
50 million premature mortalities every year (WHO, 2020). Air quality has improved substantially
51 over the past two decades in the US as the Environmental Protection Agency (EPA) observations
52 show that maximum daily 8h average (MDA8) surface ozone levels have decreased by 29% over
53 1980-2021, and annual average concentrations of particulate matter with an aerodynamic diameter
54 smaller than 2.5 μm ($\text{PM}_{2.5}$) have decreased by 37% over 2000-2021 ([https://www.epa.gov/air-](https://www.epa.gov/air-trends/air-quality-national-summary)
55 [trends/air-quality-national-summary](https://www.epa.gov/air-trends/air-quality-national-summary)). However, air pollution continues to violate the National
56 Ambient Air Quality Standards (NAAQS) in many parts of the US, such as the Colorado Front
57 Range, California, northeast US, and nearly all the national parks. A recent study reported that
58 97% of US national parks suffer from significant or unsatisfactory levels of harm from air pollution
59 (Orozco et al., 2024). Poor air quality is reported to cause about 160,000 premature deaths in the
60 US, with a total economic loss of about \$175 billion (Im et al., 2018). Exposure to air pollution
61 levels even below the EPA NAAQS can adversely affect human health (Di et al., 2017). To
62 mitigate the risks of air pollution and how air quality is responding to emission control policies, it
63 is, therefore, imperative to quantify past changes in air quality.

64 Numerous studies have revealed several key features of long-term changes in surface ozone
65 and $\text{PM}_{2.5}$ over the US using long-term observations from the EPA monitoring networks. First,
66 both the urban and rural sites in the eastern US show negative ozone trends during the summer
67 season (Butler et al., 2011; Cooper et al., 2012), but lower ozone levels at some sites have an
68 increasing trend during winter and early spring (Bloomer et al., 2010; Cooper et al., 2012; Simon



69 et al., 2015). Second, surface and free tropospheric ozone show positive trends in all seasons at
70 rural and remote sites in the western US (Jaffe and Ray, 2007; Cooper et al., 2012). Third,
71 increasing ozone is observed in the inflow to the US west coast (Jaffe et al., 2003), over the North
72 Pacific (Parrish et al., 2004), and west coast marine boundary layer (Parrish et al., 2009). The
73 Tropospheric Ozone Assessment Report (TOAR) showed that summertime surface ozone
74 continues to decrease over the US, but the trend is less certain at the urban sites (Chang et al.,
75 2017; Fleming et al., 2018). Similar regional and seasonal differences in the long-term trends are
76 also seen in PM_{2.5} and its components. For example, carbonaceous aerosols (organic and black
77 carbon) show a widespread decrease over 1990-2010 across the US in winter and spring and show
78 positive but insignificant trends over the western US (Hand et al., 2013). PM_{2.5} levels continue to
79 decrease over the majority of the US except in the wildfire-prone areas (McClure and Jaffe, 2018).

80 In addition to the observation-based trend analysis, chemical transport model (CTM)
81 simulations have been employed to interpret the observed trends. For example, the increase in
82 lower ozone values can be attributed to the increase in Asian emissions from 1980-1995 (Fiore et
83 al., 2002). The anthropogenic emissions and natural variability were found to have competing
84 effects on surface ozone over much of the US over 1980-2005 (Pozzoli et al., 2011). Another study
85 reproduced negative summertime ozone trends over the eastern US but underestimated the positive
86 trends in the western US likely due to underestimation of Asian emission trends or trans-pacific
87 transport or changes in stratosphere-troposphere exchange (Koumoutsaris and Bey, 2012). While
88 global models captured most of the observed variability and trends in summertime ozone, the use
89 of high-resolution regional models is recommended to reproduce interannual variability in winter
90 and spring in the western US (Strode et al., 2015).



91 Apart from the interpretation of observed trends, the CTMs also provide information in
92 areas with no observations. However, CTM simulations suffer from both systematic (i.e., biases)
93 and random errors due to a number of factors, including numerical approximations, inadequate
94 understanding of some processes that control the spatial and temporal distribution of air pollutants,
95 inaccuracies in the initialization of the physical and chemical atmospheric state, and uncertainties
96 in the emission inventories. While continuous efforts are being made to improve the representation
97 of processes controlling PM_{2.5} and ozone (Appel et al., 2010, 2013, 2017; Nolte et al., 2015; Fahey
98 et al., 2017) and emission inventories are updated by the EPA every three years, recent
99 developments have shown that assimilation of the National Aeronautics and Space Administration
100 (NASA) satellite retrievals of atmospheric composition in CTMs can significantly improve air
101 quality simulations (Gaubert et al., 2016; Kumar et al., 2019; Liu et al., 2011; Pagowski et al.,
102 2014; Saide et al., 2013). NASA satellite retrievals of atmospheric constituents with a far greater
103 spatial coverage compared to ground-based monitoring networks presents a unique opportunity to
104 develop long-term high-resolution air quality reanalysis, which can be useful for quantifying air
105 quality changes in unmonitored areas and assessing the impacts of changes in air quality on human
106 health and ecosystems.

107 This paper describes the methodology and evaluation of a long-term high-resolution air
108 quality reanalysis generated over the CONUS from 2005 to 2018 by assimilating the Moderate
109 Resolution Imaging Spectroradiometer (MODIS) aerosol optical depth (AOD) and the
110 Measurement of Pollution in the Troposphere (MOPITT) carbon monoxide (CO) retrievals daily
111 in the Community Multiscale Air Quality (CMAQ) model. An air quality dashboard developed to
112 enable the use of this dataset by a variety of stakeholders is also described.

113



114 **2. Methodology**

115 **2.1. The Chemical Transport Model**

116 The CMAQ model version 5.3.2 driven offline by the Weather Research and Forecasting (WRF)
117 model version 4.1 is used to simulate air quality over the CONUS from 01 Jan 2005 to 31 Dec
118 2018. We employ the “cb6r3_ae7_aq” chemical mechanism that uses Carbon Bond 6 version r3
119 for gas-phase chemistry and AERO7 aerosol module for representing aerosol processes, including
120 secondary organic aerosols (Appel et al., 2021). Both the WRF and CMAQ models use a horizontal
121 grid spacing of 12 x 12 km² with WRF (CMAQ) grid using 481 (442), 369 (265), 36 (35) grid
122 points in the longitudinal, latitudinal, and vertical directions, respectively. The model top is set to
123 50 hPa for both the models. The meteorological initial and boundary conditions for WRF are based
124 on the six hourly ERA-Interim analyses at a grid spacing of 0.7° x 0.7°. We follow Appel et al.
125 (2017) for physical parameterizations, four-dimensional data assimilation, and soil moisture
126 nudging settings in WRF. We generate meteorology-dependent anthropogenic emissions for the
127 EPA National Emissions Inventory (NEI) base years of 2011, 2014, and 2017 by feeding the WRF
128 meteorological fields to the Sparse Matrix Operator Kernel Emissions (SMOKE). The emissions
129 for 2005-2010 are derived by applying EPA reported annual state-wise trends to the NEIv2 2011
130 emissions. While NEI emissions are available for 2005 and 2008, the emissions processing
131 platform for 2005 and 2008 does not process emissions for the “cb6r3_ae7_aq” chemical
132 mechanism of CMAQ used here. Similarly, NEIv2 2014 emissions are used to derive emissions
133 for 2012 and 2013, and the NEIv1 2017 emissions are used to derive anthropogenic emissions for
134 the rest of the years. Fire emissions in CMAQ are represented using the Fire Inventory from NCAR
135 (FINN) version 2.2 which provides daily varying global fire emissions at 1 x 1 km² resolution
136 (Wiedinmyer et al., 2023). FINN emissions are processed through SMOKE to enable inline plume



137 rise of fire emissions within CMAQ. Biogenic emissions are calculated online within the model
138 using the Biogenic Emission Inventory System (BEIS). The chemical boundary conditions are
139 based on 6-hourly Whole Atmosphere Community Climate Model (WACCM) simulations (Marsh
140 et al., 2013; Gettelman et al., 2019). The WACCM output is mapped onto CMAQ grids using the
141 Initial Conditions Processor (ICON) and Boundary Conditions Processor (BCON).

142

143 **2.2. Data Assimilation System**

144 We have used the three-dimensional variational (3DVAR) capability of the community Gridpoint
145 Statistical Interpolation (GSI) version 3.5 to assimilate the Level 2 MODIS AOD retrievals and
146 the Level 2 MOPITT CO retrievals in CMAQ. The MODIS AOD assimilation framework is the
147 same as we developed previously (Kumar et al., 2019) and the MOPITT CO assimilation capability
148 has been developed in this work. We use total aerosol mass per mode (Aiken, Accumulation, and
149 Coarse) and CO mixing ratios as the control variables in GSI. The state variables include individual
150 aerosol components, total aerosol mass per mode, CO mixing ratios, meteorological variables
151 (temperature, pressure, and relative humidity), and CMAQ vertical grid. Daily MODIS and
152 MOPITT retrievals are converted into a format compatible with GSI input modules.

153 A climatological background error covariance (BEC) matrix is generated separately for
154 winter (January) and summer (July) conditions using the GEN_BE tool, which reads two different
155 WRF-CMAQ runs driven by different meteorological and emission inputs but valid at the satellite
156 overpass time. Since there are multiple overpasses of the Terra and Aqua satellites that host the
157 MOPITT and MODIS sensors, we calculate the BEC at 15 Z, 18 Z, and 21 Z. The winter BEC is
158 used when assimilating satellite retrievals from November through March and the summer BEC is
159 used for the rest of the months. Our BEC design considers the uncertainties in meteorology,



160 anthropogenic, and biomass burning emissions. Meteorological uncertainties are represented by
161 using two different sets of physical parameterizations (Table A3.1) in two WRF runs to capture
162 errors in meteorology related to assumptions used in physical parameterizations. Species-
163 dependent perturbation factors for anthropogenic and biomass burning emissions are estimated by
164 comparing a number of available global/regional anthropogenic and biomass burning emission
165 inventories over the CONUS (Table A3.2 and A3.3). Among the two WRF-CMAQ runs fed to
166 GEN_BE for BEC estimation, we used the default emissions in the first run and perturbed the
167 emissions in the second run. The BEC was then estimated in terms of variances and length scales
168 (both horizontal and vertical) for total aerosol mass per mode and CO, and used in GSI. We refer
169 the reader to Kumar et al. (2019) for a description of BEC parameters.

170 We have assimilated standard Level 2 Collection 6.1 MODIS AOD and Version 8
171 MOPITT CO retrievals based on the multispectral algorithm (thermal and near infrared) in CMAQ.
172 This multispectral product is more sensitive to near-surface CO over land compared to the thermal-
173 infrared only retrievals. MOPITT retrievals agree with in-situ measurements at all vertical levels
174 within $\pm 5\%$ (Deeter et al., 2019). The observation errors for MODIS AOD retrievals are specified
175 as $(0.03 + 0.05 * \text{AOD})$ and $(0.05 + 0.15 * \text{AOD})$ over the ocean and the land, respectively (Remer
176 et al., 2005). The observation errors for CO profiles are used as reported in the MOPITT retrieval
177 product. A simple forward operator and its adjoint based on the parameterization of (Malm and
178 Hand, 2007) is used to convert CMAQ aerosol chemical composition into AOD for a direct
179 comparison with MODIS AOD retrievals as described in Kumar et al. (2019). The forward
180 operator and its adjoint for MOPITT CO assimilation are developed in this study and described in
181 Appendix A1.

182



183 **2.3. Reanalysis production workflow**

184 Daily analyses of three-dimensional fields of aerosols and CO based on the assimilation of MODIS
185 AOD and MOPITT CO retrievals in CMAQ using the GSI system has been performed using the
186 workflow shown in Figure 1. The first CMAQ simulation on 01 Jan 2005 is initialized using the
187 global model simulations from WACCM, and all subsequent simulations until 31 Dec 2018 are
188 initialized from the previous CMAQ simulations. Every day, we perform 9 simulations, with the
189 first simulation running CMAQ from 00-15 Z, the second simulation assimilating MODIS Terra
190 and Aqua AOD retrievals at 15 Z, and third simulation assimilating MOPITT CO retrievals at 15
191 Z. The fourth simulation advances CMAQ from 15 Z to 18 Z with the fifth and sixth simulations
192 assimilating MODIS AOD and MOPITT CO at 18Z, respectively. The seventh simulation
193 advances CMAQ from 18 Z to 21 Z, the eighth simulation assimilates MODIS Aqua AOD
194 retrievals at 21 Z, and the ninth simulation advances CMAQ from 21 Z to 00 Z of the next day.
195 This resulted in a total of 46,152 jobs submission on the NCAR supercomputer Cheyenne
196 (https://arc.ucar.edu/knowledge_base/70549542). An automated script was developed to submit
197 and track successful completion of these jobs.

198 The assimilation times of 15 Z, 18 Z, and 21 Z were determined based on the analysis of
199 overpass times of Terra and Aqua satellites, which pass over the CONUS between 13:30 Z and
200 22:30 Z. All the satellite retrievals belonging to a 3-hour window are assumed to be available for
201 assimilation at the center of that window. For example, all the satellite retrievals between 1330 Z
202 and 1630 Z are assimilated at 1500 Z.

203 Our previous work has shown that the assimilation of MODIS AOD in CMAQ improved
204 the correlation coefficient between CMAQ simulated and independently observed PM_{2.5} by ~67%
205 and reduced the mean bias by ~38% over the CONUS during July 2014. To understand whether



206 GSI pushes CMAQ towards MOPITT, we performed and compared one month (July 2018) of
207 CMAQ experiments with and without assimilation of MOPITT CO profiles. We find that the
208 assimilation of MOPITT CO profiles substantially improves the correlation coefficient and reduces
209 the errors (both mean bias and root mean squared error) between CMAQ and MOPITT CO at all
210 the pressure levels except at 100 hPa where the MOPITT sensitivity is the lowest (Appendix A2,
211 Figure A2.1). This simple test confirms the ability of GSI to constrain the performance of CMAQ
212 with satellite observations. Other trace gas species (e.g., ozone and OH) are not affected directly
213 by the assimilation of AOD and CO, but the impact of assimilation indirectly affects these species
214 through photochemical processes in the model.

215

216 **2.4. Output frequency and optimization**

217 The production of a chemical reanalysis also poses a challenge of storing the model output. Since
218 our chemical reanalysis focuses on air quality applications, we saved all the chemical variables
219 together with relevant meteorological parameters (2 m temperature and relative humidity, 10 m
220 wind speed and direction, planetary boundary layer height, precipitation, and downward reaching
221 solar radiation) and deposition (both dry and wet) fluxes every hour at the surface. The total size
222 of this output is 12 Terabytes.

223

224 **3. Ground-based observations and trend calculation method**

225 We have obtained and processed hourly in-situ measurements of 2 m temperature (T2), 2 m relative
226 humidity (RH2), 10 m wind speed (WS10), 10 m wind direction (WD10), and surface pressure
227 from the METeorological Aerodrome Reports (METAR) network, which is distributed by the
228 NCEP's Meteorological Assimilation Data Ingest System (MADIS). METAR data are surface



229 weather observations and it consists of meteorological data from airports (Automated Surface
230 Observing Systems) and other permanent weather stations (Automated Weather Observing
231 System) located throughout the US. We used the Level-3 Quality Controlled METRAR data over
232 CONUS to evaluate our modeled meteorological fields
233 (https://madis.ncep.noaa.gov/madis_metar.shtml). Daily precipitation data from the 0.1-deg
234 Integrated Multi-satellitE Retrievals for Global precipitation measurements (IMERG;
235 <https://gpm.nasa.gov/data/imerg>) dataset is used to evaluate WRF simulated precipitation.

236 To evaluate the modeled surface PM_{2.5} and ozone concentrations, we have obtained hourly
237 PM_{2.5} and ozone observations from the EPA Air Quality System, which currently measures PM_{2.5}
238 and ozone at more than 1000 sites across the US. The AQS data also contains values below the
239 method detection limit (MDL). The MDLs are different for ozone and PM_{2.5} and also vary as a
240 function of site and instrument type. For consistency, we assume the MDL values of 5 ppb for
241 ozone and 2 µg/m³ for PM_{2.5} for all sites. All the data below MDL was replaced by MDL/2
242 (<https://www3.epa.gov/ttnamti1/files/ambient/airtox/workbook/AirtoxWkbk4Preparingdataforan>
243 [alysis.pdf](https://www3.epa.gov/ttnamti1/files/ambient/airtox/workbook/AirtoxWkbk4Preparingdataforan); <https://pubs.acs.org/doi/10.1021/es071301c>). The sites for which two simultaneous
244 measurements (corresponding to two instruments) were available, the mean value is taken for
245 further calculation.

246 The trend calculations were performed using both the observed and modeled ozone and
247 PM_{2.5} values. The monthly mean time series of observed and modeled maximum daily 8-hour
248 (MDA8) ozone and 24-hour average PM_{2.5} during 2005-2018 is calculated over all measurement
249 sites. The daily MDA8 ozone over a site is calculated using the EPA's defined methodology
250 (<https://www.govinfo.gov/content/pkg/FR-2015-10-26/pdf/2015-26594.pdf>, pp 168). For each
251 day, 8-hour running averages are taken from 7 am to 11 pm local standard time, which constitutes



252 17 8-hour running mean values per day. If an 8-hour window has less than 6 hours of data and the
253 mean value of the remaining hours is less than 70 ppb then the data for that window is discarded.
254 If a site has fewer than 13 valid 8-hour mean values or the maximum value of the available 8-hour
255 average is less than 70 ppb then the value for that day is discarded. For PM_{2.5}, a daily 24-hour
256 average value is calculated in local standard time only if at least 18 hours of valid data/day are
257 available. Furthermore, we discarded all sites with (1) < 50% data per month, (2) < 50 % data
258 during each year, and (3) if number of years with $\geq 50\%$ data were < 10 years during 2005-2018.
259 The number of valid sites fulfilling the above criteria over CONUS are estimated to be 1012 and
260 369, for MDA8 ozone and 24-hour PM_{2.5}, respectively. Daily values of MDA8 ozone and 24-hour
261 PM_{2.5} are used to calculate monthly 5th percentile, 50th percentile, 95th percentile and mean time
262 series during 2005-18 at each valid site. A similar criterion for seasonal mean, 5th, 50th and 95th
263 percentile time series was also used. The number of valid sites during summer season were the
264 maximum (1010/357 for MDA8 O₃/24-hour PM_{2.5}) and were minimum (501/337 for MDA8
265 O₃/24-hour PM_{2.5}) during the winter season. These annual and seasonal MDA8 ozone and PM_{2.5}
266 time series are then used to estimate annual and seasonal trends and the significance of trend values
267 are also tested.

268

269 **4. Results and Discussions**

270 **4.1. Meteorological evaluation**

271 The WRF simulations for the entire period (2005-2018) processed using the Meteorology-
272 Chemistry Interface Processor (MCIP) are collocated with METAR observations of T2, RH2,
273 WS10, and WD10 in space and time, and paired values are used for evaluating the model. The
274 evaluation is performed at a regional scale following the EPA regional classification of the



275 CONUS in 10 regions. The number of METAR sites during 2005-2018 was 1290, and the
276 maximum available hourly data during the study period was 33-68 % over 10 EPA regions. Region
277 8 has the least data (~33-37%), and other regions have 47-68 % data during 2005-2018. Hourly
278 regional averaged model and METAR observations time series are compared over 10 EPA regions
279 for T2 (Figure 2), RH2 (Figure 3), WS10 (Figure 4), and WD10 (Figure 5). Three statistical
280 metrics, namely correlation coefficient (r), mean bias (MB), and root mean square error (RMSE),
281 for each region are also listed in Figures 2-5.

282 Hourly regional averaged T2 between model and observations (Figure 2) show excellent
283 correlations of 0.8-1.0 with low mean biases of -0.3 to 0.4 °C and the RMSE ranging from 2.0-5.7
284 °C over the 10 EPA regions. The model also performed well ($r = 0.7-0.9$) in simulating RH2
285 (Figure 3) over 10 EPA regions with the mean biases of 0.9-3.6 % and the RMSE of 12.5 - 16.3
286 %. Since RH2 is estimated as a ratio of vapor pressure to saturation pressure (e_s) and e_s depends
287 on T2, the biases in T2 also contribute to the biases in RH2. For example, EPA Region 6 which
288 shows the highest T2 RMSE also shows the highest RH2 RMSE. The model reproduces the
289 variations in surface pressure very well ($r = 1.0$) with a slight underestimation (MB = -8.1 to 0.2
290 hPa; RMSE = 0.3-8.1 hPa). The slight underestimation in pressure is seen in eight out of 10 EPA
291 regions with the largest MB in Regions 9 (-8.1 hPa) and 10 (-7.4 hPa). The errors in surface
292 pressure (plot not shown) over these regions could also contribute to biases in T2 and RH2.

293 Prior to 10 m wind speed comparison, model wind speeds are assigned “zero value” if the
294 hourly wind speed at any site is less than 0.51 m/s (1 knot). This step was needed to make model
295 output consistent with the METAR wind speed data, which treats such wind speeds as calm winds
296 and assigns it a zero value. Our model simulation slightly overestimates (MB = 0.1-0.8 m/s) WS10
297 (Figure 4) over most of EPA regions with the exception of Region 8 (MB = -0.1 m/s). Wind



298 direction (Figure 5) biases (absolute) over these regions were 34°-58°. The correlation coefficients
299 for both WS10 and WD10 are slightly lower in Regions 8-10, which is likely due to the complex
300 topography in these regions. The correlation coefficients for 10 m wind speed were lower than
301 those for temperature, and relative humidity, indicating a slightly poorer model performance for
302 winds. The WRF model is known to overpredict 10 m wind speed at low to moderate wind speeds
303 in all available planetary boundary layer (PBL) schemes (Mass and Ovens, 2010). This
304 shortcoming of the model was partly attributed to unresolved topographical features by the default
305 surface drag parameterization, which in turn influences surface drag and friction velocity, and
306 partly to the use of coarse horizontal and vertical resolutions of the domain (Cheng et al., 2005).

307 Since WRF and IMERG precipitation have different resolutions, we first mapped the WRF
308 simulated precipitation from a 12 km x 12 km grid on Lambert conformal projection to the IMERG
309 rectilinear grid of 0.1° x 0.1° using the “rcm2rgrid” functionality of the NCAR command language
310 (<https://www.ncl.ucar.edu/Document/Functions/Built-in/rcm2rgrid.shtml>). The seasonal mean
311 WRF simulated and IMERG derived precipitation are then compared over four seasons during
312 2005-2018 (Figure 6). The model is able to capture the spatial patterns in precipitation in different
313 seasons, with an underestimation of -0.1 to -0.9 mm/day. The highest underestimation is observed
314 during the winter season. The eastern CONUS showed an underestimation during winter, spring
315 and autumn seasons, however, over the western US, the model mostly overestimated the
316 precipitation, especially in the mountainous regions (Rockies, Cascades, and Sierra Nevada). The
317 model also showed larger biases over the lakes and oceanic regions. Despite the biases, this
318 comprehensive evaluation shows that our model simulations captured the key features of regional
319 and temporal variability of the key meteorological parameters over the CONUS fairly well.

320



321 4.2. Air Quality evaluation

322 Hourly regional averaged observed and CMAQ simulated surface ozone and PM_{2.5} are
323 compared for all the EPA regions in Figures 7 and 8, respectively. In all the regions, the model
324 captures the seasonal cycle in surface ozone characterized by a summertime peak as well as the
325 observed interannual variability very well, with correlation coefficients of 0.77 to 0.91. The model
326 also overestimates the nighttime ozone levels in all the regions, but a larger overestimation is seen
327 in Regions 8 and 9. The mean bias and RMSE in modeled ozone are very similar across the regions,
328 with values ranging from 3.7 - 6.8 ppbv and 7.0-9.0 ppbv, respectively. The model shows a slightly
329 poorer skill in capturing the variability in PM_{2.5} relative to ozone as reflected by smaller r values
330 of 0.49-0.79 but captures long-term trends in most of the regions reasonably well. The mean bias
331 and RMSE in modeled PM_{2.5} are estimated to be -0.9 to 5.6 µg/m³ and 3.0 to 8.3 µg/m³,
332 respectively. The largest underestimation of PM_{2.5} is seen in Region 8, particularly from 2005 to
333 2012 while the largest overestimation is seen in Region 2.

334 In addition to regional evaluation, we also evaluated the model performance for different
335 land use types and location settings (see Appendix A2, Figure A2.2 for classification of the number
336 of sites in these categories). This categorization information by land use and location types was
337 not available for a very small number of sites, and thus, they were excluded from the analysis (sites
338 classified as “NONE” in Figure A2.2). Since Maximum Daily Averaged 8-hour (MDA8) ozone
339 and daily averaged PM_{2.5} are policy-relevant metrics, we focus on the evaluation of these
340 parameters on a monthly averaged scale for this evaluation. We evaluate monthly median (50th
341 percentile), 5th and 95th percentile time series of MDA8 ozone, and daily averaged PM_{2.5} for
342 different land use categories and location settings (Appendix A2, Figures A2.3-A2.8).



343 Among the rural sites, all land use categories showed the highest biases for the 5th
344 percentile, followed by the median and 95th percentile for MDA8 ozone, except for the “Others”
345 category, for which the median showed the lowest bias. For suburban and urban site types, 95th
346 percentile MDA8 ozone consistently showed the lowest bias for all land use types, followed by
347 the median and 5th percentile. Furthermore, “Others” land use category under the rural and urban
348 sites shows the lowest bias for 5th percentile and the median, while “residential” land use type
349 shows the lowest bias for the suburban sites.

350 For PM_{2.5}, the largest differences between the model and observations are seen for the 95th
351 percentile at “Others” land use categories compared to the 5th percentile and median. The model
352 generally captures the temporal variability in PM_{2.5} across all land use types (except “Others”) and
353 location settings for all three-percentile metrics analyzed here but some anomalies are also evident.
354 For example, residential and commercial sites in the urban category show larger overestimation
355 for the median and 95th percentiles during 2005-2006, indicating higher uncertainties in
356 anthropogenic emission estimates at these sites during these years. While the model follows most
357 of the observed peaks in 95th percentile, it substantially underestimates the observed peaks.

358 The errors in air quality simulations can be attributed to the uncertainties in different types
359 of emissions used to drive air quality models, errors in the lateral boundary conditions representing
360 pollution inflow, uncertainties in meteorological parameters (as quantified earlier in this section),
361 and poor understanding of some of the physical and chemical processes controlling the fate of
362 those emissions. To quantify uncertainties in anthropogenic and biomass burning emissions over
363 the CONUS, we compared all available anthropogenic and biomass burning emission inventories
364 over the CONUS and found that anthropogenic emission estimates across various emission
365 inventories vary by a factor of 1.16 - 2.94 (Table A3.2) and the corresponding fire emission



366 estimates vary by 3.13 - 8.0 (Table A3.3). The extrapolation of the NEI emissions to years other
367 than the base years might have also introduced some uncertainties in our simulations because EPA
368 reported state level trends may not always represent local (sub-state) changes in emissions and
369 also do not provide information about new emission sources appearing in the CONUS between
370 two NEI base emission inventory years.

371

372 **4.3. Trend analysis**

373 The spatial distribution of positive/negative trend values in MDA8 ozone and 24-hr average PM_{2.5}
374 calculated using monthly median values in AQS and CMAQ data during 2005-2018 are shown in
375 Figures 9 and 10, respectively. Different symbols are used to represent urban, suburban, and rural
376 site types. Based on location, ~42/23% of sites were in rural areas, ~41/45 % in suburban areas
377 and ~17/32% were in urban or city centers, respectively, for MDA8 ozone/24-hr average PM_{2.5}.
378 Darker/lighter red and blue colors represent statistically significant/insignificant increasing and
379 decreasing trends at 2-sigma level. Over the study period, both the model and observations show
380 decreasing trends in MDA8 ozone over the majority of the CONUS. Most eastern US sites show
381 decreasing trends that were statistically significant with p values less than 0.05. The sites located
382 in western/northwestern US, however, showed mixed results with some sites showing increasing
383 trends, most of which were not statistically significant. Similar results were observed during the
384 summer season with most sites showing statistically significant decreasing trends over the most
385 locations. During autumn and winter seasons, several sites over California and the eastern US
386 showed decreasing but insignificant trends. Some sites over the midwestern US also changed the
387 trend sign during these seasons. The trends in winter seasons were mostly positive (increasing,
388 55% agreement between AQS and CMAQ) over most sites in the US (except for the coastal sites



389 in the southeastern US). The number of sites with negative trend values in summer changed from
390 3% to 55% positive trends during winter season. Most of these trends, however, were not
391 statistically significant and the number of sites was also reduced to about 560% of the sites
392 available for annual evaluation during this season. The seasonal changes in monthly median trends
393 discussed above were mostly consistent (67-86%) between the AQS and CMAQ data. A similar
394 analysis with 5th and 95th percentile time series suggested that the higher percentiles showed mostly
395 decreasing trends, but 5th percentile dataset at the mid-western US, Boston-New York-DC, and
396 central US sites showed increasing trends on a seasonal and annual basis. The MDA8 ozone trend
397 over CONUS (1012 sites) is estimated to be $-0.53 \pm 0.46/-0.56 \pm 0.45$ ppb/year (summertime) and
398 $-0.31 \pm 0.43/-0.29 \pm 0.39$ ppb/year (annual), respectively, for AQS/CMAQ data, with most sites
399 (~70 %) showing negative trends. At the 2-sigma level (p -value < 0.05), the summertime mean
400 ozone trends are $-0.85 \pm 0.36/-0.75 \pm 0.35$ ppb/year for 484/620 sites and annual MDA8 ozone
401 trends are $-0.52 \pm 0.45/-0.47 \pm 0.42$ ppb/year for 554/562 sites, respectively, for AQS/CMAQ data
402 over CONUS. This suggests decreases in monthly high ozone days but increases in monthly low
403 ozone. On an annual basis, MDA8 ozone showed the most decreasing trends (AQS/CMAQ = -0.40
404 $\pm 0.37/-0.34 \pm 0.34$ ppb/year) in the 428 rural sites. The mean ozone trends over urban (411 sites)
405 and suburban (170) areas were (AQS/CMAQ = $-0.28 \pm 0.44/-0.29 \pm 0.40$ ppb/year) and
406 (AQS/CMAQ = $-0.13 \pm 0.48/-0.15 \pm 0.48$ ppb/year), respectively. The ozone trends over high-
407 altitude sites (16 sites), are mostly negative for AQS/CMAQ = $-0.43 \pm 0.45/-0.12 \pm 0.36$ ppb/year)
408 in summer and annually (AQS/CMAQ, = $-0.39 \pm 0.38/-0.03 \pm 0.29$ ppb/year).

409 Similar MDA8 ozone trends were also reported in a previous study (Simon et al., 2015).
410 Mousavinezhad et al. (2023) reported that all regions except the Northern Rockies and the
411 Southwest experienced decreasing trends in median MDA8 ozone values during the warm season



412 of 1991-2020, with rural stations in the Southeast and urban stations in the Northeast experiencing
413 the greatest declines of -1.29 ± 0.07 ppb/year and -0.85 ± 0.08 ppb/year, respectively. They also
414 reported a large decrease in MDA8 ozone 95th percentile in all regions. Similarities in ozone trends
415 between the AQS observations and CMAQ simulations over a longer time period 1990-2015 is
416 also reported by He et al. (2020).

417 On an annual basis, 24-hr average $PM_{2.5}$ also showed mostly decreasing trends ($\sim 79\%$)
418 over most of the sites. A majority of these trends were also statistically significant at 2-sigma level
419 (AQS/CMAQ = 70%/75%). However, unlike MDA8 ozone, an increasing trend (though
420 insignificant) in summertime $PM_{2.5}$ is observed over the north-western US (Fig. 9). The wintertime
421 trends were also mostly decreasing over most of the sites, except for the northwestern US. During
422 summer season about 5-fold increase (annual $\sim 5\%$; summer $\sim 24\%$) in positive trends is observed
423 in high $PM_{2.5}$ days (95th percentile time series) and most of these increases were observed over the
424 Pacific Northwest. These summertime increases in $PM_{2.5}$ trends are also evident from the 95th
425 percentile time series, where a sharp increase in $PM_{2.5}$ is observed during 2017-2018 overall sites
426 except industrial locations (refer to Fig. S8). In recent years these changes could be even stronger
427 as wildfire activity over the western US has increased in the last decade. The dramatic decreasing
428 trends of $PM_{2.5}$ in the eastern US were also reported in previous studies (Zhang et al., 2018; Gan
429 et al., 2015; Xing et al., 2015) (Gan et al., 2015; Xing et al., 2015; Zhang et al., 2018) due to
430 emission reductions. The increasing trend in the western central area is due in part to frequent
431 wildfires (Dennison et al., 2014; McClure and Jaffe, 2018). For $PM_{2.5}$ the overall mean trends are
432 -0.24 ± 0.21 / -0.24 ± 0.24 $\mu\text{g}/\text{m}^3/\text{year}$ (369 sites) in AQS/CMAQ data sets. Unlike, MDA8 ozone,
433 the number of sites remained almost the same (337-357 sites in four seasons, 369 annual) during
434 seasons and an overall negative trend is also observed (-0.18 ± 0.25 to -0.30 ± 0.35 $\mu\text{g}/\text{m}^3/\text{year}$).



435 At 2-sigma level, the number of sites that showed negative trends in both the datasets were 69-80
436 %.

437 On an annual basis, the mean PM_{2.5} trends over urban sites are $-0.17 \pm 0.22/-0.18 \pm 0.15$
438 $\mu\text{g}/\text{m}^3/\text{year}$, suburban sites are $-0.28 \pm 0.22/-0.24 \pm 0.26$ $\mu\text{g}/\text{m}^3/\text{year}$ and -0.3 $\mu\text{g}/\text{m}^3/\text{year}$, and urban
439 and city center are $-0.23 \pm 0.21/-0.30 \pm 0.27$ $\mu\text{g}/\text{m}^3/\text{year}$ $\mu\text{g}/\text{m}^3/\text{year}$, respectively, for AQS/CMAQ
440 data. The only high-altitude site for PM_{2.5} showed an increase in the annual ($0.07/0.06$ $\mu\text{g}/\text{m}^3/\text{year}$
441 for AQS/CMAQ data) and summertime trend ($0.13/0.13$ $\mu\text{g}/\text{m}^3/\text{year}$ for AQS/CAMQ data).
442 During other seasons, mostly low negative trends were observed. The ozone trends over high-
443 altitude sites (16 sites), however, are mostly negative ($-0.43 \pm 0.45/-0.12 \pm 0.36$ ppb/year in
444 summer and $-0.39 \pm 0.38/-0.03 \pm 0.29$ ppb/year, annually). The ozone trends at high altitude sites
445 showed large seasonal variations with min to max ranges of -0.69 to $0.87/-1.5$ to 0.26 ppb/year for
446 AQS/CMAQ data.

447

448 **4.4. Air Quality dashboard**

449 The comprehensive evaluation of our reanalysis in the above sections shows that our
450 reanalysis is able to capture key features of long-term trends in both MDA8 ozone and PM_{2.5} over
451 most parts of the CONUS. This increases confidence in using this dataset for assessing the trends
452 in unmonitored areas of the CONUS. Therefore, a Geographic Information System (GIS)-based
453 dashboard has been developed to aid in community engagement and understanding of the
454 reanalysis data. The dashboard was developed using Esri ArcGIS Dashboard technology (Esri,
455 2024). An interactive web-based dashboard allows stakeholders to explore air quality annual
456 concentrations and the number of days that exceed a certain threshold over space and time. It
457 provides a step-by-step path for users to explore information at the CONUS, state, and county



458 levels. In the center of the dashboard is a time series chart showing trends in annual concentrations
459 of MDA8 ozone, NO₂, PM_{2.5}, PM₁, and PM₁₀ between 2005 and 2018. An indicator element of a
460 dashboard highlights how many days between 2005 and 2018 have exceeded the National Ambient
461 Air Quality Standards (NAAQS) for ozone and PM_{2.5}, and a bar chart graph shows the number of
462 days that exceeded the NAAQS each year. There is also a map that zooms to the selected state or
463 county of interest and illustrates the spatial distribution of air quality variables using a quantitative
464 color bar.

465 The dashboard can be used to better understand how particular events, such as large
466 wildfires, have affected air quality in certain geographic areas. For example, the 2008 wildfires in
467 Shasta and Trinity Counties in California, referred to as the June Fire Siege, had a major impact
468 on air quality (<https://storymaps.arcgis.com/stories/c6535ee477e14b72a20393a5f10aefbc>). Figure
469 11 shows MDA8 ozone concentrations for Shasta County, California. The dashboard shows a
470 sharp increase in MDA8 ozone concentration in 2008, as depicted in the time series plot. The bar
471 chart in the lower right corner also reflects the large number of days that exceeded the NAAQS
472 criteria for MDA8 ozone in 2008.

473 The dashboards also can be used to visualize the efficacy of air quality management
474 policies. For example, Los Angeles County, CA has designed and implemented strict emission
475 standards to improve air quality. Figure 12 shows the downward trend in PM_{2.5} concentrations in
476 Los Angeles County during 2005-2018. The air quality dashboard is publicly accessible at
477 <https://ncar.maps.arcgis.com/apps/dashboards/9a97650dc77b4f7192b99ea9bef36a21>.

478 We have also developed a Python-based Streamlit application allowing users to select and
479 download data for specific time periods aggregated over administrative boundaries such as cities,
480 counties, and states. Temporal and spatial aggregations are performed on the server, and only



481 information of interest is downloaded and delivered to the users, taking the data processing
482 workload off of the users. The Streamlit application allows users to select a time period, a temporal
483 aggregation (daily, weekly, monthly, annual), one or more air quality variables, statistics (min,
484 mean, max), and an area of interest (state, county, city). The data can then be downloaded as a
485 comma-separated file as well as graphed on the website as seen in Figure 13. The Streamlit
486 application is available at: <https://compass.rap.ucar.edu/airquality/>

487

488 **5. Data availability**

489 The global meteorological datasets used to drive WRF are publicly available through National
490 Center for Atmospheric Research (NCAR) Research Data Archive (<https://rda.ucar.edu/>). The
491 SMOKE setup used to create emissions for CMAQ is accessible via EPA emissions modeling
492 platform (<https://www.epa.gov/air-emissions-modeling/emissions-modeling-platforms>). FINN
493 biomass burning emissions can be downloaded from <https://rda.ucar.edu/datasets/ds312.9/>.
494 Meteorological observations used to evaluate the model performance are downloaded from
495 <https://madis-data.cprk.ncep.noaa.gov/madisPublic1/data/archive/>. The EPA AQS system
496 observations are downloaded from <https://www.epa.gov/aqs>. Hourly surface output from the
497 WRF-CMAQ-GSI system can be downloaded from <https://doi.org/10.5065/cfya-4g50> (Kumar and
498 He, 2023)

499

500

501

502 **6. Code availability**



503 The WRF, CMAQ, and GSI source codes are publicly accessible at <https://github.com/wrf-model/>,
504 <https://github.com/USEPA/CMAQ>, and [https://dtcenter.org/community-code/gridpoint-](https://dtcenter.org/community-code/gridpoint-statistical-interpolation-gsi/download)
505 [statistical-interpolation-gsi/download](https://dtcenter.org/community-code/gridpoint-statistical-interpolation-gsi/download).

506

507 7. Conclusions

508 Air pollution is an important health hazard affecting human health and the economy in the CONUS
509 but still, millions of people in counties with no monitors. To address this gap and help air quality
510 managers understand long-term changes in air qualities at the county level across the CONUS, we
511 have created a 14-year long 12-km hourly dataset by daily assimilation of atmospheric composition
512 observations from the NASA MODIS and MOPITT sensors aboard the Terra and Aqua satellites
513 in the Community Multiscale Air Quality (CMAQ) model from 01 Jan 2005 to 31 Dec 2018. The
514 WRF model has been used to simulate meteorological parameters, which are then used to drive
515 CMAQ offline and for generating meteorology-dependent anthropogenic emissions.

516 The meteorological parameters, ozone, and PM_{2.5} have been extensively validated against
517 multi-platform observations to characterize uncertainties in our dataset, which air quality managers
518 need to determine the confidence they can put in our dataset. We show that our dataset captures
519 regional scale hourly, seasonal, and interannual variability in the meteorological variability well
520 across the CONUS. The model shows an excellent performance in simulating the regional and
521 temporal variability in temperature and relative humidity but a slightly poorer performance in
522 simulating winds and precipitation, which are well known shortcomings of the WRF model. The
523 model also shows a higher skill in reproducing variabilities in surface ozone ($r = 0.77-0.91$) than
524 PM_{2.5} ($0.49-0.79$). The mean biases for CMAQ ozone and PM_{2.5} are estimated to be 3.7-6.8 ppbv



525 and -0.9 - $5.6 \mu\text{g}/\text{m}^3$, respectively, and the corresponding RMSE values are 7-9 ppbv and 3.0-8.3
526 $\mu\text{g}/\text{m}^3$, respectively.

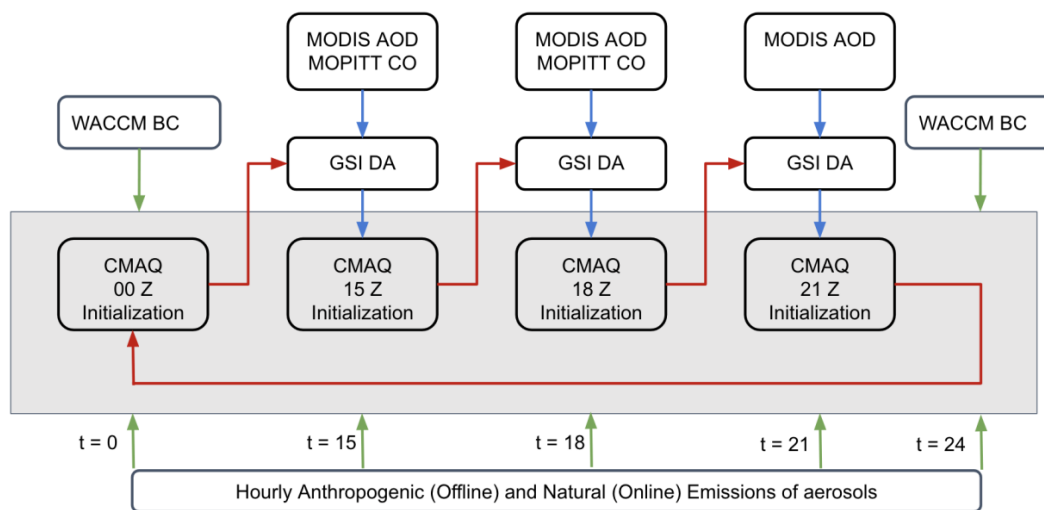
527 The MDA8 ozone trend over CONUS is estimated to be -0.53 ± 0.46 / -0.56 ± 0.45 ppb/year
528 (summertime) and -0.31 ± 0.43 / -0.29 ± 0.39 ppb/year (annual), respectively, for AQS/CMAQ data
529 with ~70% of sites showing negative trends. At a 2-sigma level, the summertime MDA8 ozone
530 trends are -0.85 ± 0.36 / -0.75 ± 0.35 ppb/year and annual MDA8 ozone trends are -0.52 ± 0.45 /
531 0.47 ± 0.42 ppb/year, respectively, for AQS/CMAQ data over CONUS. Annually, at 2-sigma level,
532 46% sites showed negative trends in both the data. Annual mean $\text{PM}_{2.5}$ trends are -0.24 ± 0.21 /
533 $0.24 \pm 0.24 \mu\text{g}/\text{m}^3/\text{year}$, respectively in AQS/CMAQ data sets, and ~79% of the sites showed
534 negative trends. Annually, at 2-sigma level, 66% sites showed negative trends in both the data.
535 During summertime, the negative trend percent is reduced to 71%, where an increase in positive
536 trends are observed in the northwestern US.

537 An air quality dashboard has been developed, which provides a step-by-step path for users
538 to explore information at the CONUS, state, and county levels. This dashboard allows the users to
539 visualize air quality information in the form of maps, bar charts, and the NAAQS exceedance days.
540 Finally, a Python-based Streamlit application is developed to allow the download of the air quality
541 data in simplified text and graphic formats for the end user's choice of the region and time of
542 interest.

543



544 8. Figures



545

546 **Figure 1:** Architecture of the daily GSI/CMAQ based chemical data assimilation workflow.

547

548

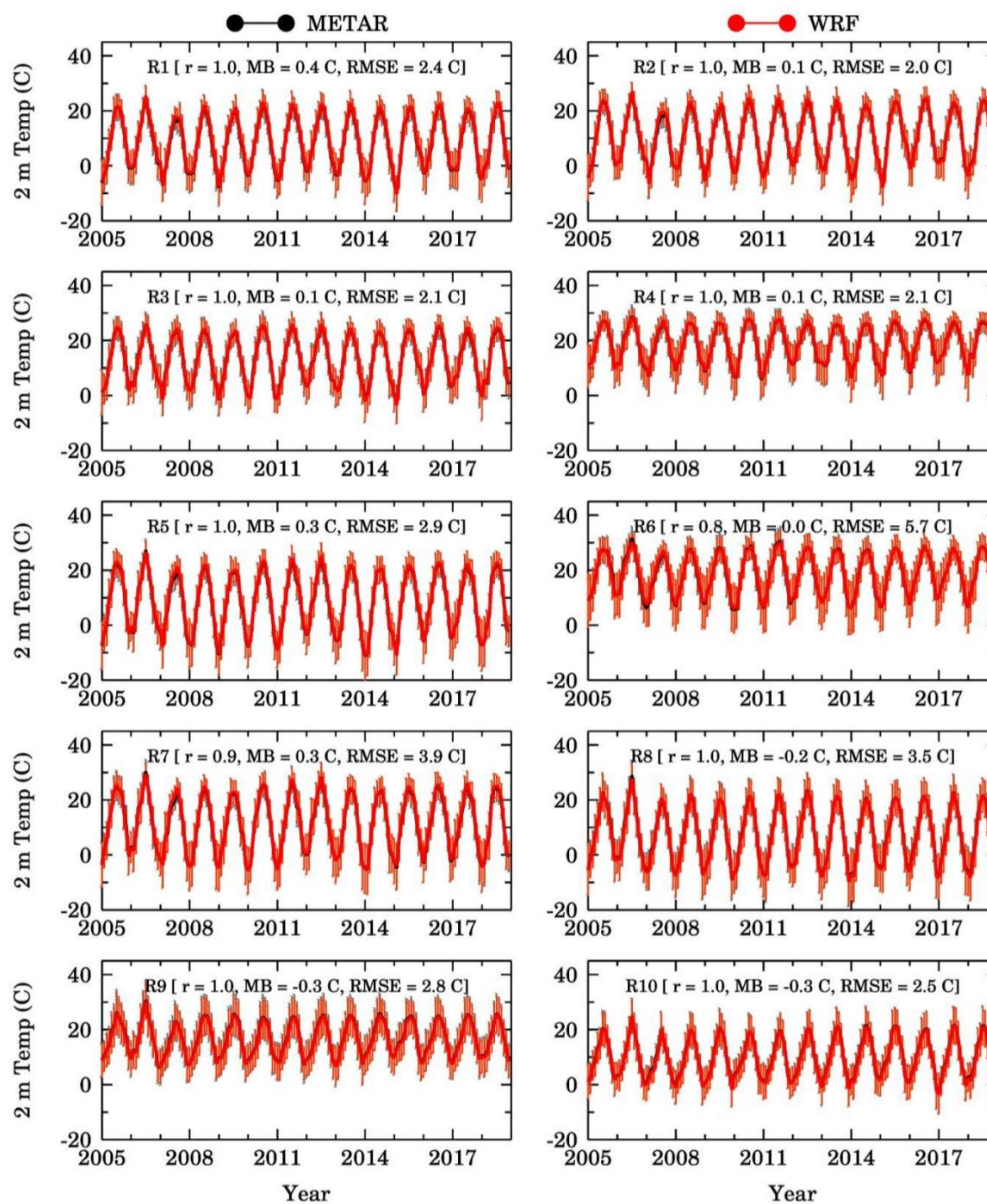
549

550

551

552

553

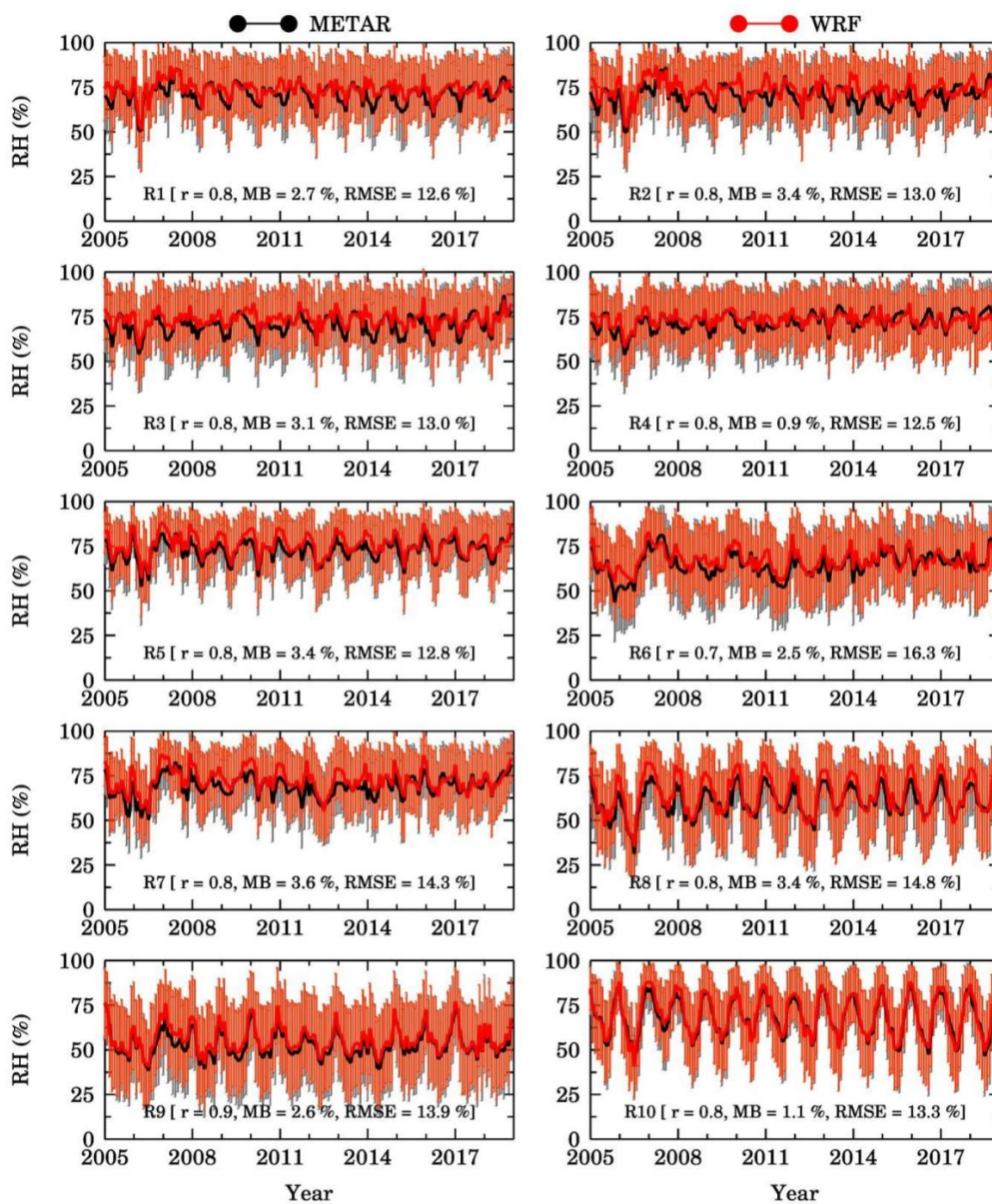


554

555 **Figure 2:** Time series of hourly averaged 2 m temperature over 10 EPA regions (R1-R10) from
556 WRF-CMAQ setup (red) and METAR observations (black) during 2005-2018. Orange and Grey
557 lines represent the standard deviation for WRF-CMAQ and METAR, respectively. The correlation



558 coefficient (r), mean bias (MB), and the root mean square error (RMSE) for each region is also
559 shown.
560

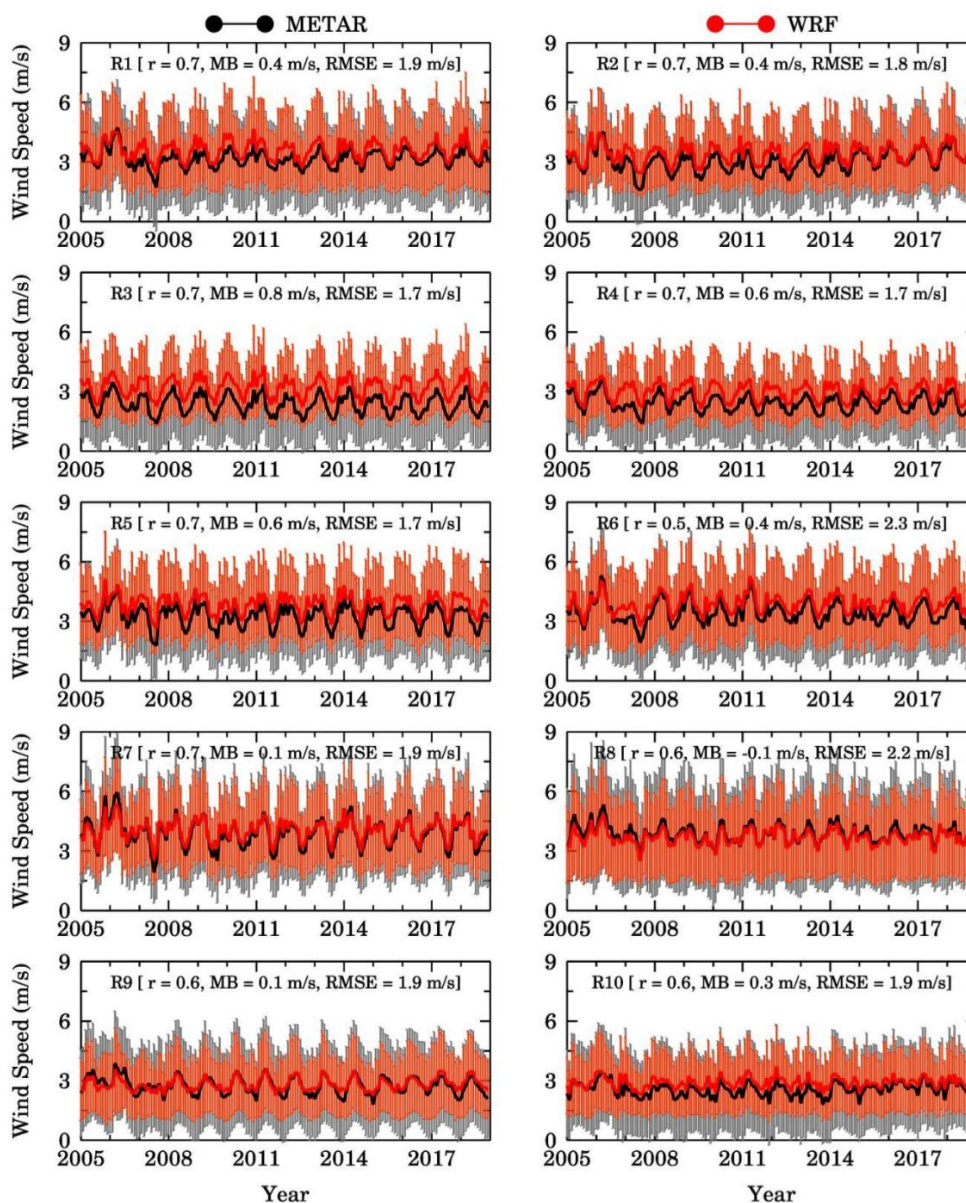


561



562 **Figure 3:** Same as Figure 2 but for 2 m relative humidity.

563



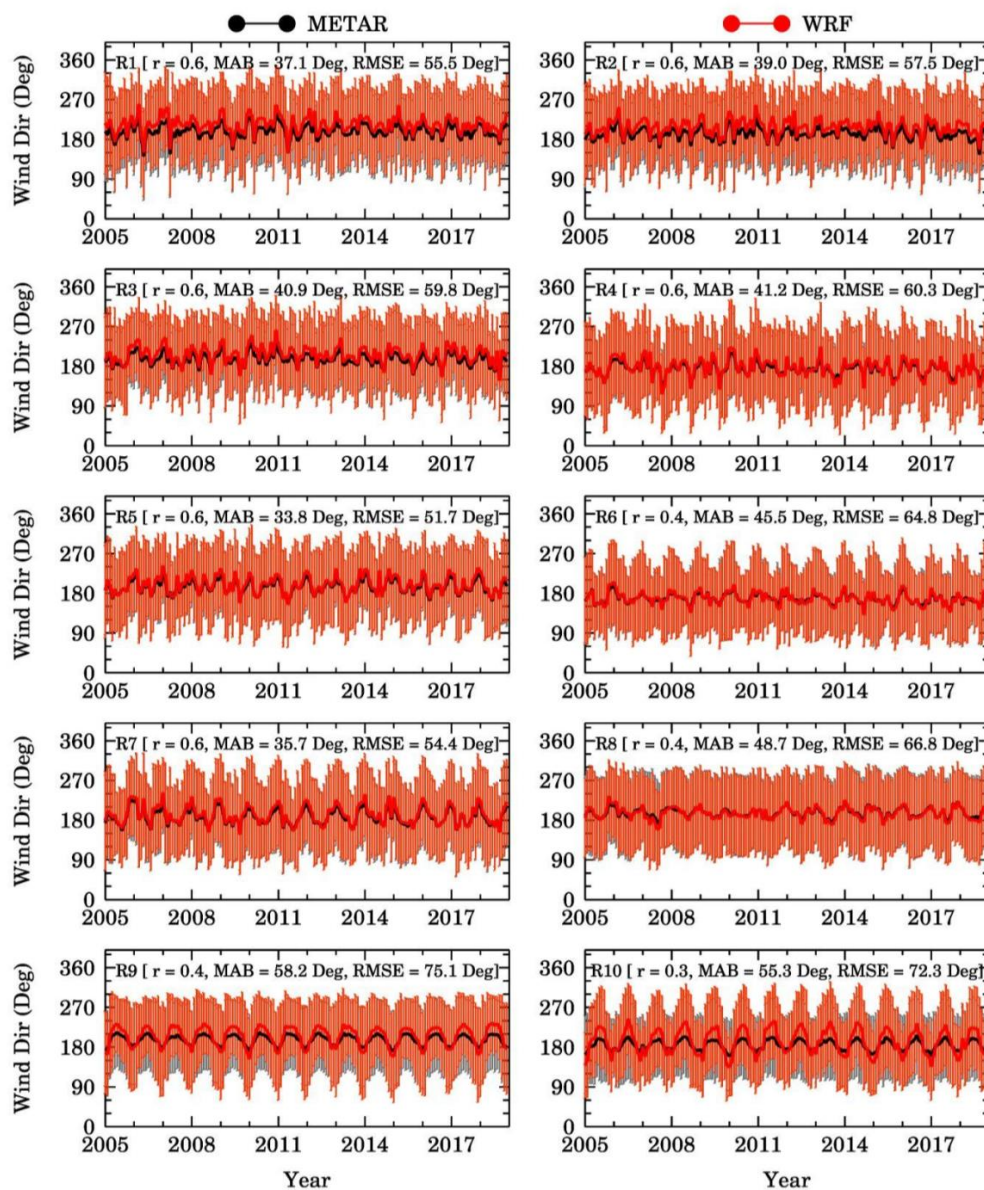
564

565 **Figure 4:** Same as Figure 2 but for 10 m wind speed.



566

567

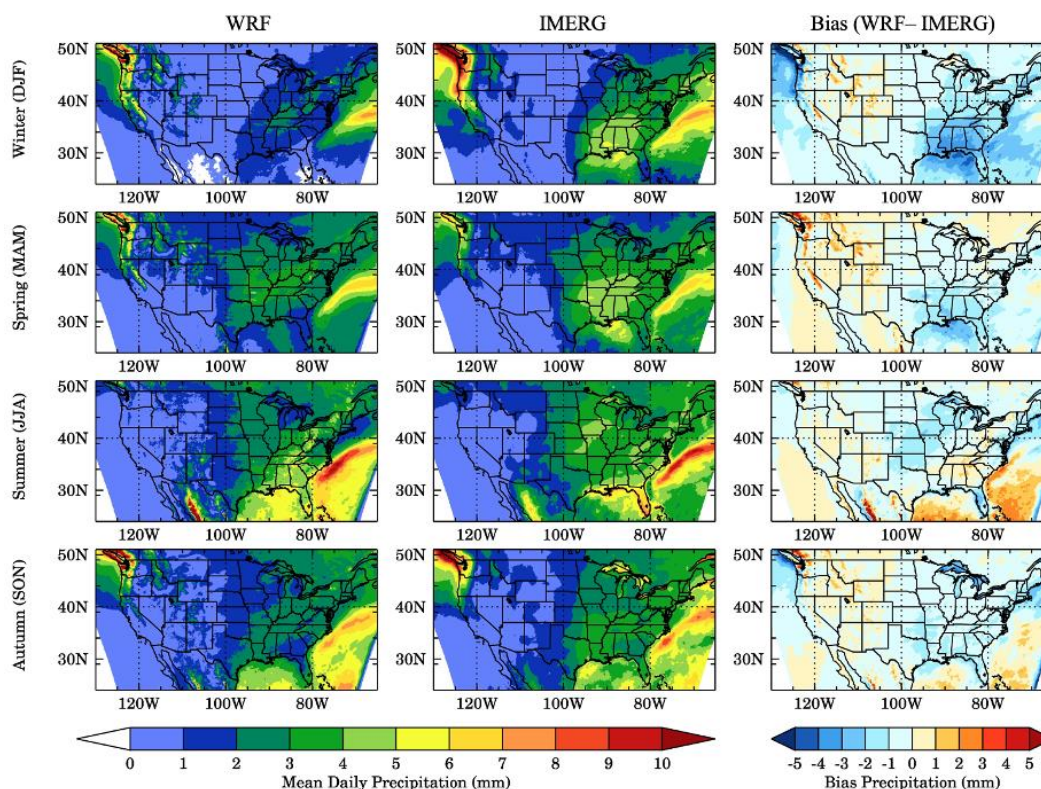


568

569 **Figure 5:** Time series of hourly averaged 2 m temperature over 10 EPA regions (R1-R10) from
570 WRF-CMAQ setup (red) and METAR observations (black) during 2005-2018. Orange and Grey



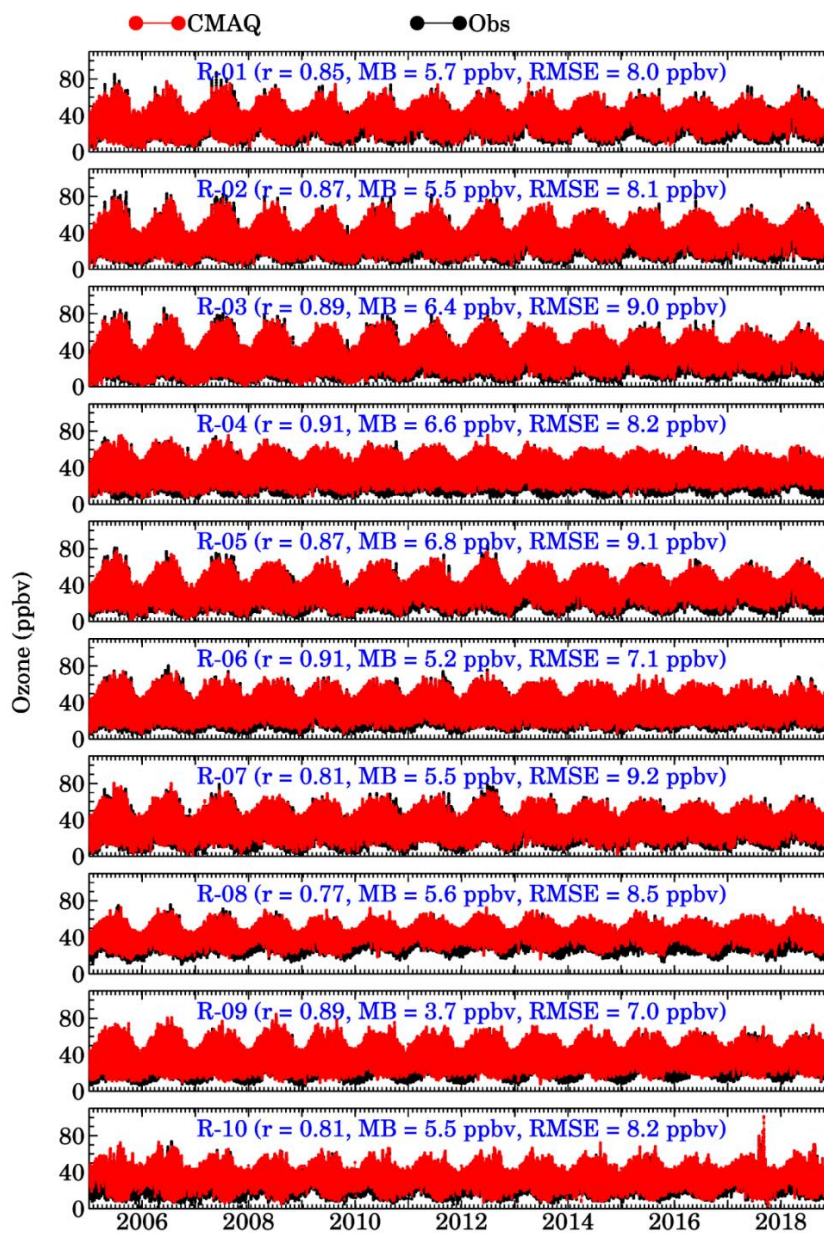
571 lines represent standard deviation for WRF-CMAQ and METAR, respectively. The correlation
572 coefficient (r), mean absolute bias (MAB), and the root mean square error (RMSE) for each region
573 is also shown.



574

575 **Figure 6:** Spatial distribution of mean daily precipitation and bias during four seasons in 2005-
576 2018 (top to bottom, *viz.*, Winter, Spring, Summer and Autumn). Left, center and right panels
577 represent mean precipitation from WRF, IMERG and bias (WRF-IMERG) precipitation,
578 respectively.

579

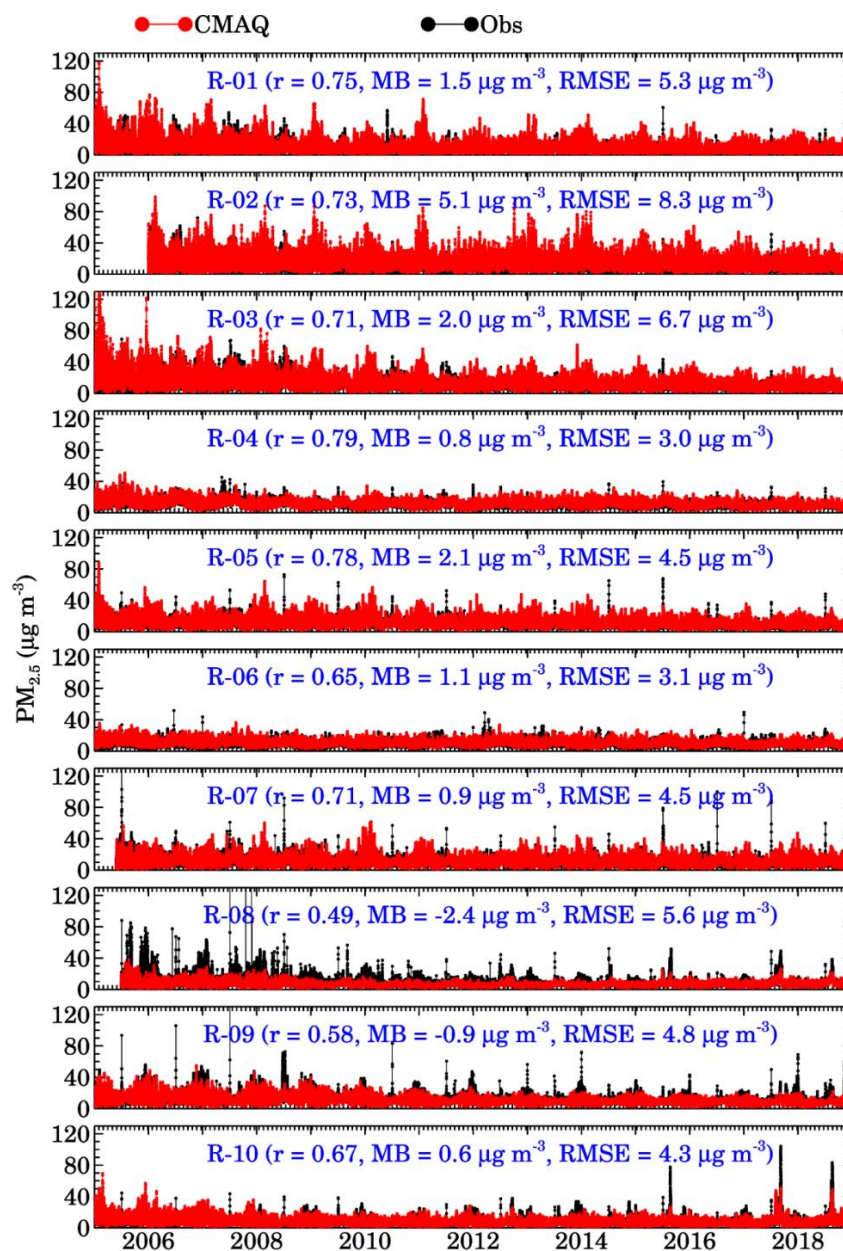


580

581 **Figure 7:** Time series of hourly averaged surface ozone over 10 EPA regions (R1-R10) from
582 WRF-CMAQ setup (red) and EPA AQS observations (black) during 2005-2018. The correlation



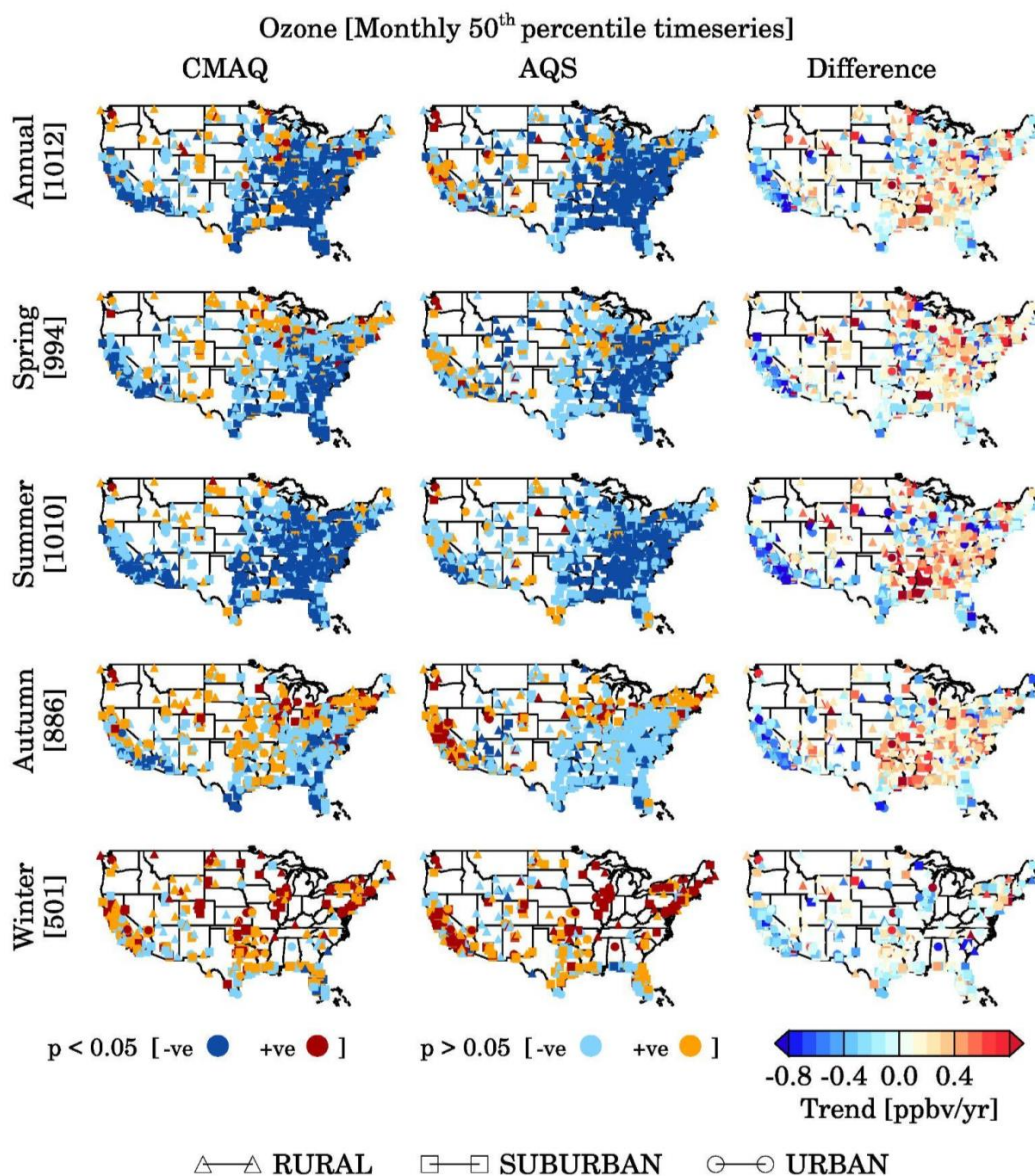
583 coefficient (r), mean bias (MB), and the root mean square error (RMSE) for each region is also
584 shown.
585



586

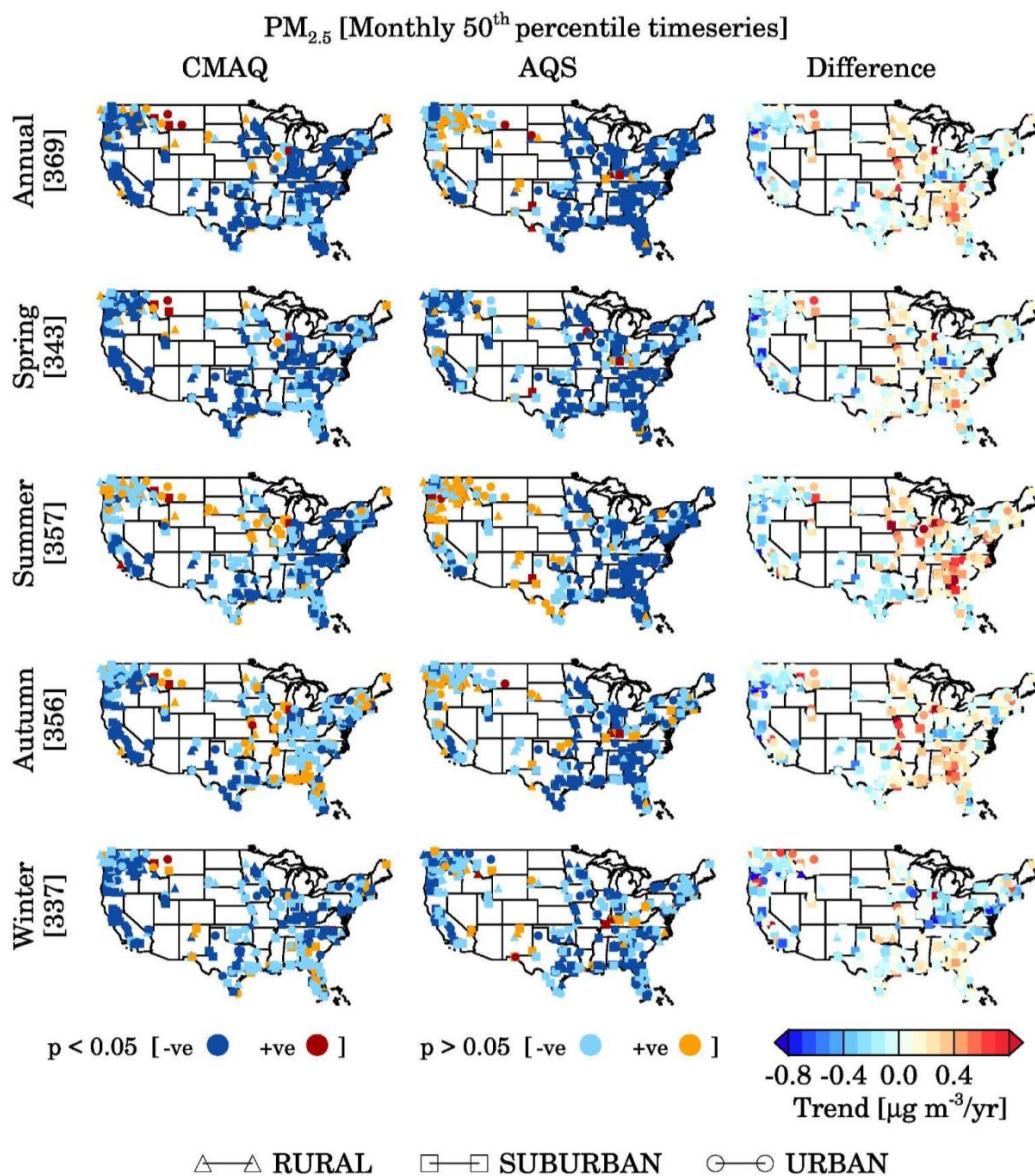


587 **Figure 8:** Same as Figure 7 but surface fine particulate matter ($PM_{2.5}$).



588

589 **Figure 9:** Spatial distribution of positive (blue colors), negative trends (red colors) in MDA8 ozone
 590 at different statistically significant levels (p-values) using annual, seasonal monthly median time
 591 series (top to bottom). Plots on the right show differences in trend values [CMAQ-AQS].



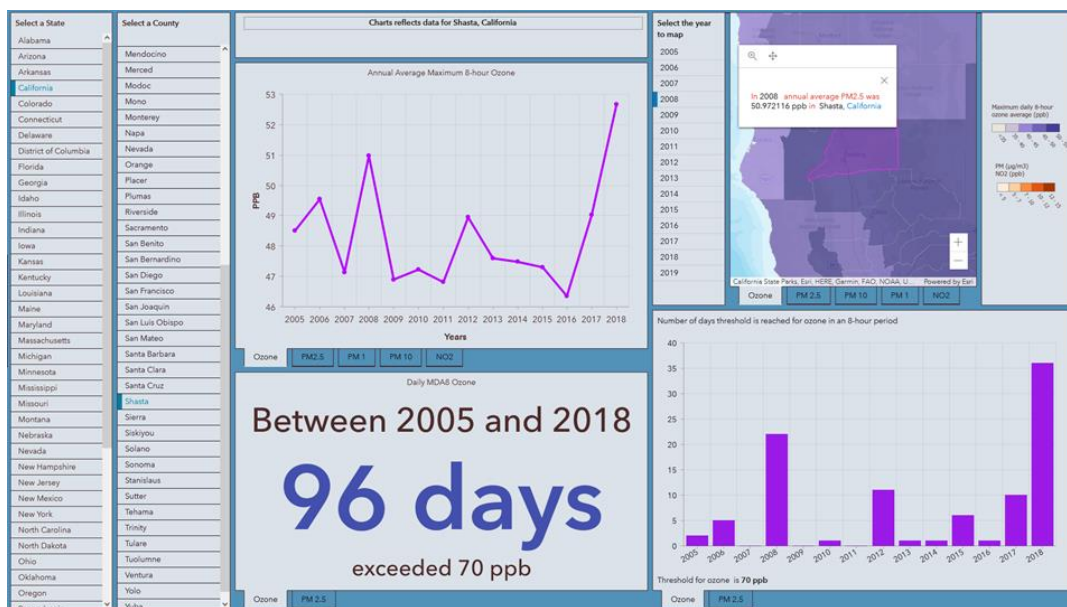
592

593 **Figure 10:** Spatial distribution of positive (blue colors), negative trends (red colors) in 24-hour

594 avg. PM_{2.5} (right panel) at different statistically significant levels (p-values) using monthly median

595 time series (top to bottom). Plots on the right show differences in trend values [CMAQ-AQS].

596



597

598 **Figure 11:** Dashboard reflecting Ozone concentrations for Shasta, CA.

599

600

601

602

603



604

605 **Figure 12:** PM_{2.5} concentrations for Los Angeles, CA.

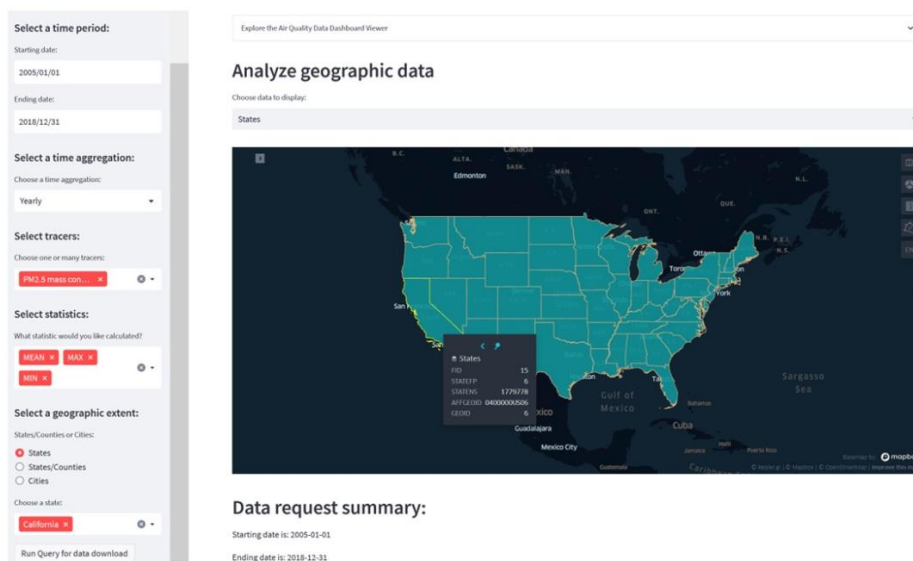
606

607

608

609

610



611

612 **Figure 13:** Streamlit Air Quality App to easily download and summarize data in a CSV format.

613

614

615



616 **9. Appendices**

617 **A1: Forward and Adjoint operators for MOPITT CO assimilation**

618 MOPITT retrieved profile consists of 10 levels, including a surface level followed by 100 hPa
 619 thick layers from 900 hPa to 100 hPa. The CMAQ vertical profile of CO cannot be compared with
 620 MOPITT CO directly and needs to be convolved with the MOPITT a priori profile and averaging
 621 kernel. Following (Barré et al., 2015; Gaubert et al., 2016), the CMAQ profile that can be
 622 compared directly to MOPITT can be written as:

623
$$CO_{ret}^{CMAQ} = 10^{(AK^{MOPITT} \log_{10}(CO^{CMAQ}) + (I - AK^{MOPITT}) \log_{10}(CO_{apr}^{MOPITT}))} \quad (1)$$

624

625 CO_{ret}^{CMAQ} is the CMAQ CO profile convolved with MOPITT a priori averaging kernel (AK^{MOPITT})
 626 and a priori profile (CO_{apr}^{MOPITT}) that can be compared directly to the MOPITT retrieved CO profile.

627 CO^{CMAQ} is the 10-layer CMAQ profile mapped to the MOPITT pressure grid. A
 628 \log_{10} transformation is necessary because the averaging kernel matrix for retrievals is obtained
 629 with CO parameters in $\log_{10}(CO)$. Differentiation of equation (1) will yield the sensitivity of

630 CO_{ret}^{CMAQ} with respect to CO^{CMAQ} , which represents the adjoint of the forward operator. For the
 631 purpose of derivation, let $CO_{ret}^{CMAQ} = y$; $CO^{CMAQ} = x$; $AK^{MOPITT} = A$; and $(I -$
 632 $AK^{MOPITT}) \log_{10}(CO_{apr}^{MOPITT}) = C$ then equation (1) can be written as:

633
$$y = 10^{(A \log_{10}(x) + C)} \quad (2)$$

634 Applying the differentiation rule $\frac{d[a^u]}{dx} = \ln(a) \cdot a^u \cdot \frac{du}{dx}$; we can differentiate equation (2) as:

635
$$\frac{dy}{dx} = \ln(10) \cdot 10^{(A \log_{10}(x) + C)} \cdot \frac{d}{dx} (A \log_{10}(x) + C) \quad (3)$$

636 Since A and C do not depend on CMAQ simulations, they are constants and thus their
 637 differentiation is zero. Since $\frac{d}{dx} (\log_{10}(x)) = \frac{1}{x \ln(10)}$, equation (3) simplifies to



638
$$\frac{dy}{dx} = 10^{(A \log_{10}(x) + C)} \cdot A \cdot \frac{1}{x} = A \cdot \frac{y}{x} \quad (4)$$

639 Substituting the values of $y, x, A,$ and C in equation (4), the changes in CO vertical profile in the
640 MOPITT space can be related to changes in CO vertical profile in CMAQ as follows:

641
$$dCO_{ret}^{CMAQ} = AK^{MOPITT} \cdot \frac{CO_{ret}^{CMAQ}}{CO^{CMAQ}} dCO^{CMAQ} \quad (5)$$

642 By writing equation (5) in matrix form and then transposing the forward operator matrix, we can
643 write the adjoint of the forward operator as a recursive matrix equation:

644
$$dCO^{CMAQ} = dCO_{ret}^{CMAQ} + AK^{MOPITT} \cdot \frac{CO_{ret}^{CMAQ}}{CO^{CMAQ}} dCO_{ret}^{CMAQ} \quad (6)$$

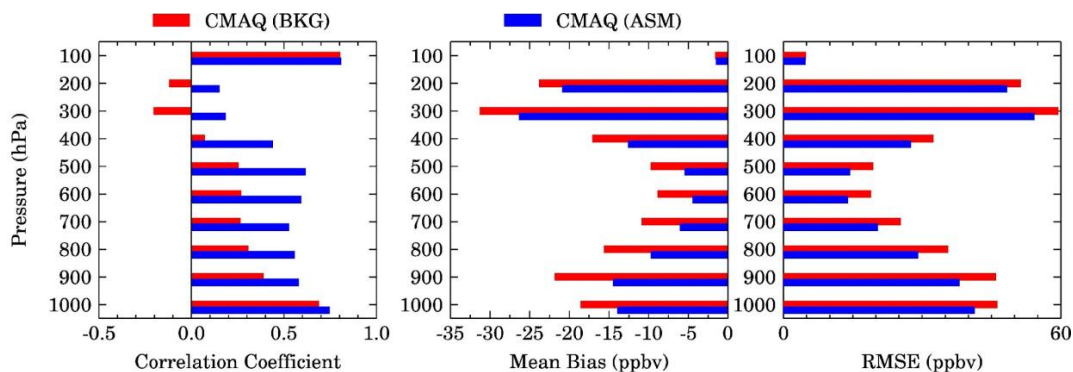
645

646



647 **A2: Additional Figures**

648



649

650 **Figure A2.1:** Correlation coefficient, Mean bias, and Root Mean Squared Error (RMSE)

651 between CMAQ and MOPITT CO profiles at ten MOPITT retrievals pressure levels for the

652 CMAQ experiments with (ASM) and without (BKG) assimilation of the MOPITT CO profiles

653 during July 2018. These statistics are based on 118552 data points at each level.

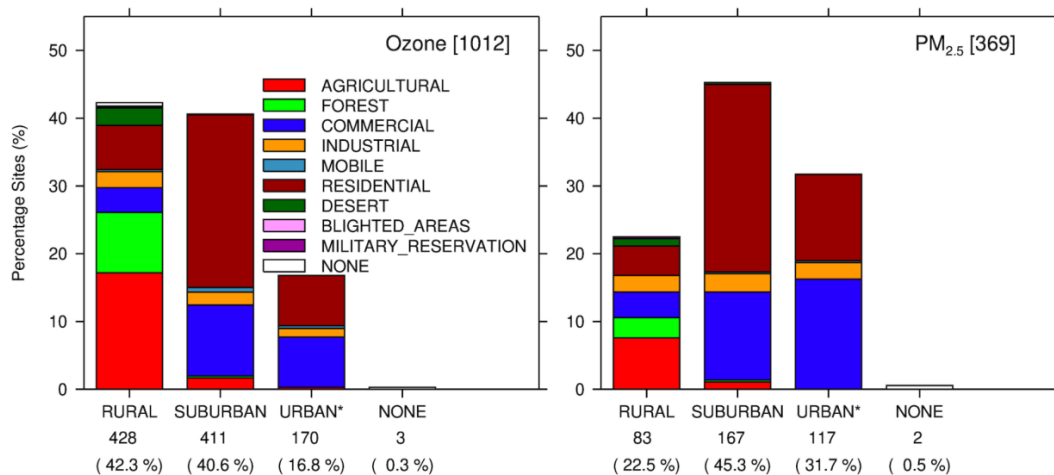
654

655

656

657

658



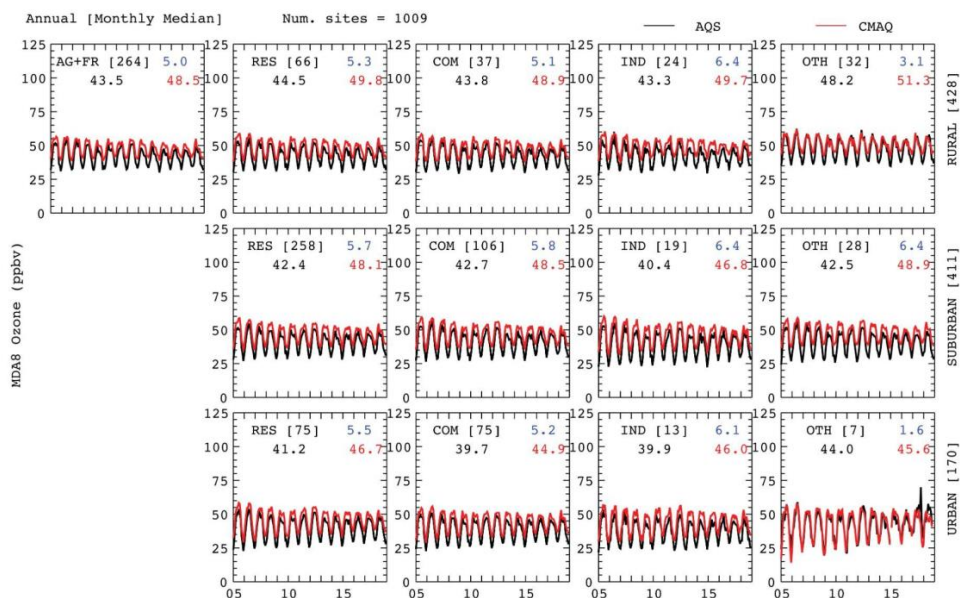
659

660 **Figure A2.2:** The stacked histogram shows the number of sites in each location setting (different
 661 bars) and land use type (different colors) for MDA8 ozone (left) and 24-hr avg. PM_{2.5} (right).

662

663

664

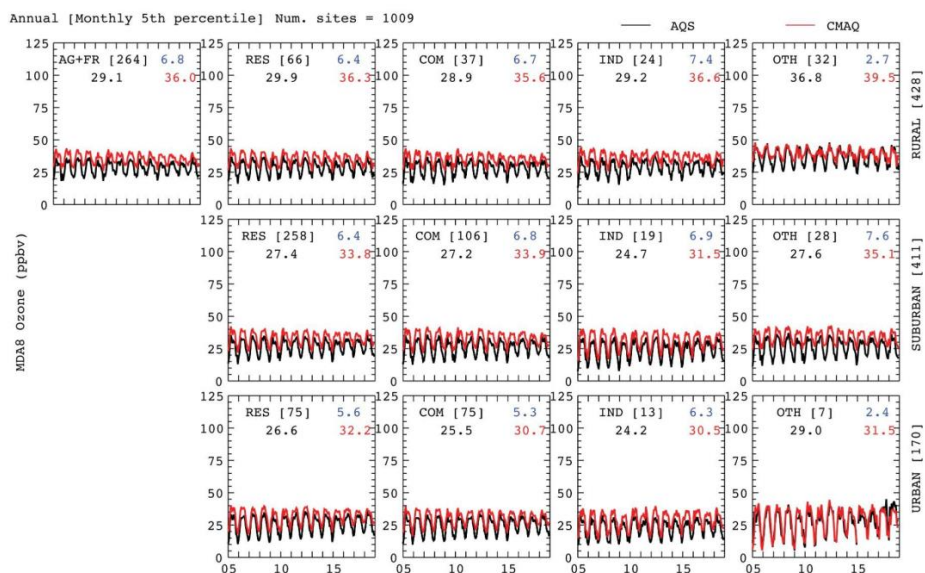


665

666 **Figure A2.3:** The Annual mean (derived from monthly median values) time series of MDA8
667 Ozone using AQS data (black) and CMAQ (red) over different location type (top to bottom) and
668 land-use type (left to right) during 2005-2018. The number of sites for each scenario are presented
669 in brackets. The blue color represents the mean bias.

670

671

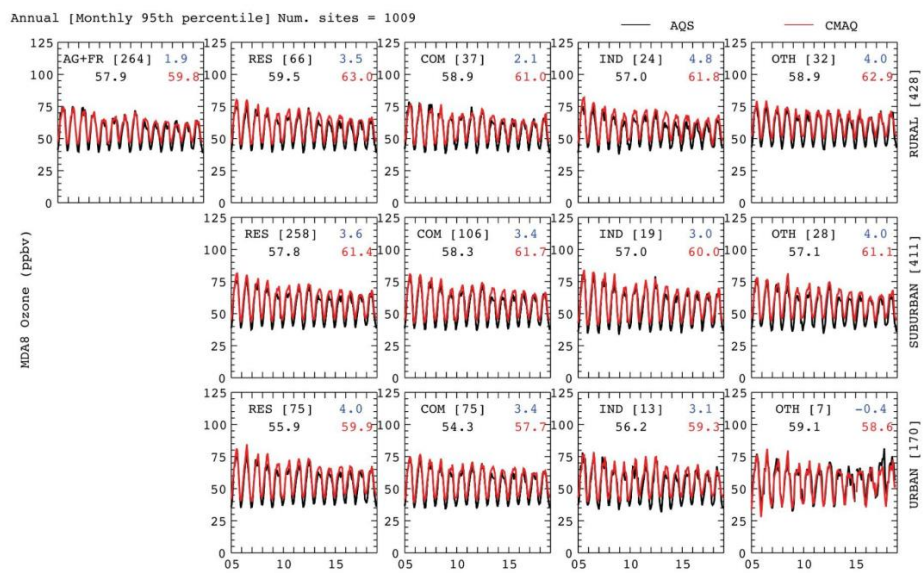


672

673 **Figure A2.4:** Same as Figure A2.3 but time series is derived from monthly 5th percentile values

674

675

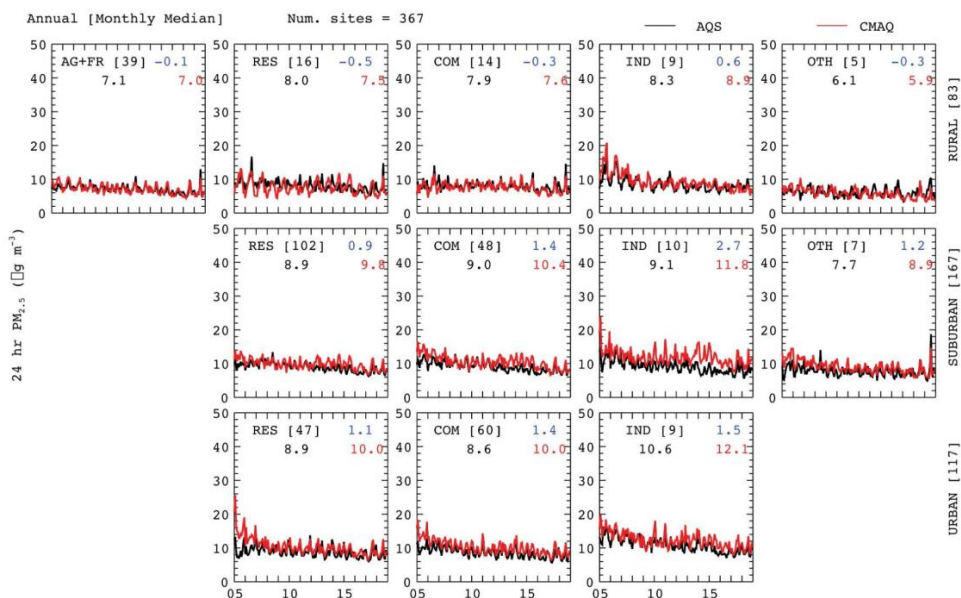


676

677 **Figure A2.5:** Same as Figure A2.3 but time series is derived from monthly 95th percentile values.

678

679

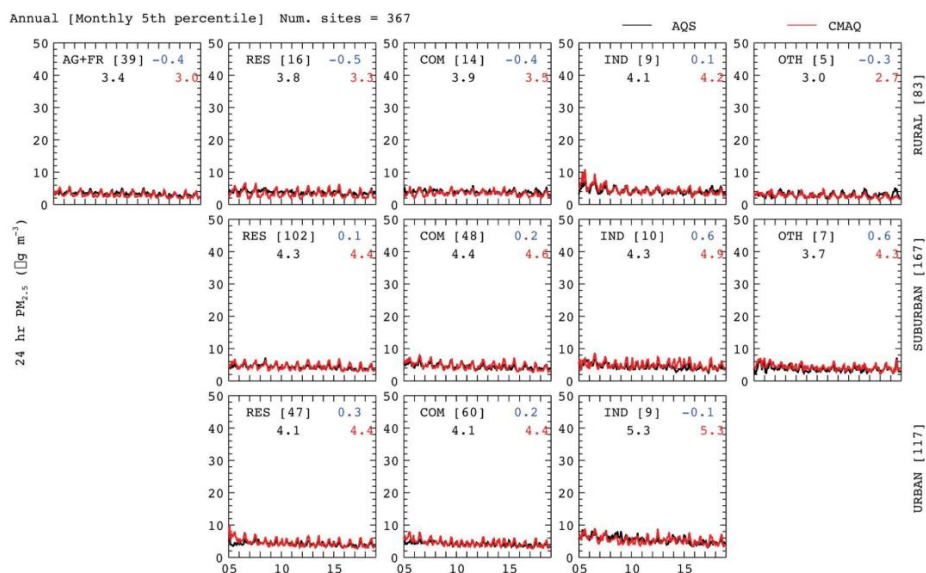


680

681 **Figure A2.6:** The Annual mean (derived from monthly values) time series of 24-hour avg. $PM_{2.5}$
682 using AQS data (black) and CMAQ (red) over different location types (top to bottom) and land-
683 use type (left to right) during 2005-18. The number of sites for each scenario are presented in
684 brackets. The blue color represents the mean bias.

685

686

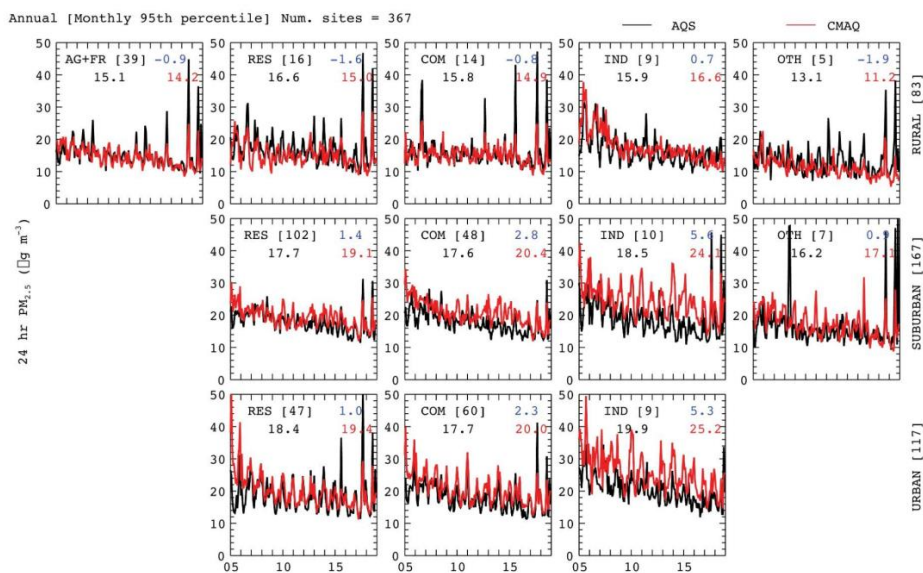


687

688 **Figure A2.7:** Same as Figure A2.6 but time series is derived from monthly 5th percentile values.

689

690



691

692 **Figure A2.8:** Same as Figure A2.6 but time series is derived from monthly 95th percentile values.

693

694

695

696

697

698

699

700

701

702

703

704



705 **A3: Additional Tables**

706 **Table A3.1:** Key physics and chemical schemes used in the WRF-CMAQ configuration.

Physics	Setup-1 (standard simulation used for assimilation)	Setup-2 (sensitivity simulation used to generate background error)
Long-wave radiation	RRTMG	RRTM Longwave
Short-wave radiation	RRTMG	Goddard Shortwave
Microphysics	Morrison double-moment	Thomson
Cumulus	Kain–Fritsch version 2	Grell 3-D ensemble
Land surface model	Pleim–Xiu LSM	Unified Noah LSM
Surface Layer	Pleim–Xiu surface layer	MYNN
PBL	ACM2	MYNN level 2.5
Gas-phase chemistry	CB06	CB06
Aerosol chemistry	AERO7	AERO7
Anthropogenic and fire emissions	EPA NEI	EPA NEI perturbed by factors* derived from uncertainty analysis of multiple emission datasets
Biogenic emission	Online CMAQ BEIS	Offline MEGAN

707



709 **Table A3.2:** Annual anthropogenic emissions for nine species over CONUS during 2005-2018.

Emissions (Tg/yr)	HTAP v2 [2010]	EDGAR v4.3.2 [2010]	MACCity [2005-16]	CAMSv4.2 [2005-16]	NEI+ [2014]	Min-Max Ratio
CO	56.20	56.77	46.02 ± 6.39	56.49 ± 6.46	45.69	1.24
NH₃	4.42	5.14	4.44 ± 0.14	5.12 ± 0.07	3.25	1.58
NO_x	11.07	10.93	10.40 ± 1.00	10.46 ± 0.96	12.03	1.16
SO₂	13.10	12.52	10.87 ± 2.44	11.48 ± 1.90	4.46	2.94
CH₂O	0.12	0.20	0.17 ± 0.02	0.26 ± 0.02	0.16	2.17
NMVOC	15.61	14.57	6.58 ± 0.82	14.92 ± 0.74	12.28	2.37
OC	0.61	0.36	0.48 ± 0.08	0.36 ± 0.01	0.79**	2.19
BC	0.34	0.20	0.28 ± 0.06	0.21 ± 0.02	0.26**	1.70
PM_{2.5}	2.02	N/A	N/A	N/A	3.67	1.82

710 ⁺ Except NEI, all other emissions are simply summed over {20-50 N} & {60-130 W} region

711 ** CONUS PM_{2.5} emissions are 5.15 Tg/yr which has 8% BC (or EC) and 28% OC

712 https://www.epa.gov/sites/production/files/2019-08/documents/210pm_rao_508_2.pdf

713

714



715 **Table A3.3:** Annual biomass burning emissions for nine species over the CONUS during 2005-
 716 2018.

Emissions (Tg/yr)	Top-Down emissions		Bottom-up emissions			Min-Max Ratio
	QFED	GFASv1.3	FINNv1.5	GFEDv4.1	NEI	
CO	12.90 ± 2.59	8.99 ± 2.40	10.93 ± 2.21	5.41 ± 1.12	16.95	3.13
NH₃	0.56 ± 0.11	0.12 ± 0.03	0.18 ± 0.04	0.07 ± 0.02	0.27	8.00
NO_x	0.56 ± 0.11	0.20 ± 0.06	0.47 ± 0.10	0.18 ± 0.04	0.25	3.11
SO₂	0.32 ± 0.07	0.07 ± 0.02	0.09 ± 0.02	0.04 ± 0.01	0.13	8.00
CH₂O	0.16 ± 0.03	0.15 ± 0.04	0.15 ± 0.03	0.10 ± 0.02	0.22	2.20
tVOC	0.53 ± 0.11	1.05 ± 0.28	1.86 ± 0.40	1.06 ± 0.22	3.92	7.40
OC	2.99 ± 0.63	0.60 ± 0.17	0.66 ± 0.13	0.34 ± 0.09	0.45	8.79
BC	0.24 ± 0.05	0.05 ± 0.02	0.06 ± 0.01	0.03 ± 0.01	0.15	8.00
PM_{2.5}	4.37 ± 0.92	0.90 ± 0.24	N/A	0.61 ± 0.14	1.48	7.16

717



718 **10. Author contribution**

719 RK, PB, CH, GGP, SA, HW, and OG conceptualized the study. All the authors contributed to the
720 design of the study. RK, CH, and PB performed all the model simulations including the data
721 assimilation system developments and experiments. PB, CH, RK, and SA contributed to the model
722 evaluation and trend analysis. RK, FL, JB, OG, KS, MC, and SS contributed to the design of the
723 air quality dashboard and Streamlit application. RK prepared the first draft of the paper. All authors
724 contributed to the editing of the manuscript.

725

726 **11. Competing interests**

727 The authors do not have any competing interests. The funding agency had no role in the design of
728 the study, in the collection, analyses, interpretation of data, in the writing of the manuscript,
729 or in the decision to publish the results.

730

731 **12. Financial support**

732 This work is supported by the NASA Atmospheric Composition Modeling and Analysis
733 (ACMAP) Grant # 80NSSC19K0982.

734

735 **13. Acknowledgement**

736 We would like to acknowledge high-performance computing support from Cheyenne (doi:
737 10.5065/D6RX99HX (accessed on 08 June 2023)), provided by NCAR's Computational and
738 Information Systems Laboratory, sponsored by the National Science Foundation. The National
739 Center for Atmospheric Research is sponsored by the National Science Foundation under
740 Cooperative Agreement 1852977.



743

744 **14. References**

- 745 Appel, K. W., Bash, J. O., Fahey, K. M., Foley, K. M., Gilliam, R. C., Hogrefe, C., Hutzell, W.
746 T., Kang, D., Mathur, R., Murphy, B. N., Napelenok, S. L., Nolte, C. G., Pleim, J. E.,
747 Pouliot, G. A., Pye, H. O. T., Ran, L., Roselle, S. J., Sarwar, G., Schwede, D. B., Sidi, F.
748 I., Spero, T. L., and Wong, D. C.: The Community Multiscale Air Quality (CMAQ)
749 model versions 5.3 and 5.3.1: system updates and evaluation, *Geoscientific Model*
750 *Development*, 14, 2867–2897, <https://doi.org/10.5194/gmd-14-2867-2021>, 2021.
- 751 Appel, K. W., Napelenok, S. L., Foley, K. M., Pye, H. O. T., Hogrefe, C., Luecken, D. J., Bash,
752 J. O., Roselle, S. J., Pleim, J. E., Foroutan, H., Hutzell, W. T., Pouliot, G. A., Sarwar, G.,
753 Fahey, K. M., Gantt, B., Gilliam, R. C., Heath, N. K., Kang, D., Mathur, R., Schwede, D.
754 B., Spero, T. L., Wong, D. C., and Young, J. O.: Description and evaluation of the
755 Community Multiscale Air Quality (CMAQ) modeling system version 5.1, *Geoscientific*
756 *Model Development*, 10, 1703–1732, <https://doi.org/10.5194/gmd-10-1703-2017>, 2017.
- 757 Appel, K. W., Pouliot, G. A., Simon, H., Sarwar, G., Pye, H. O. T., Napelenok, S. L., Akhtar, F.,
758 and Roselle, S. J.: Evaluation of dust and trace metal estimates from the Community
759 Multiscale Air Quality (CMAQ) model version 5.0, *Geoscientific Model Development*, 6,
760 883–899, <https://doi.org/10.5194/gmd-6-883-2013>, 2013.
- 761 Appel, K. W., Roselle, S. J., Gilliam, R. C., and Pleim, J. E.: Sensitivity of the Community
762 Multiscale Air Quality (CMAQ) model v4.7 results for the eastern United States to MM5
763 and WRF meteorological drivers, *Geoscientific Model Development*, 3, 169–188,
764 <https://doi.org/10.5194/gmd-3-169-2010>, 2010.



- 765 Atmospheric Environment, Volume 300, 2023, 119693, ISSN 1352-2310,
766 <https://doi.org/10.1016/j.atmosenv.2023.119693>.
- 767 Barré, J., Gaubert, B., Arellano, A. F. J., Worden, H. M., Edwards, D. P., Deeter, M. N.,
768 Anderson, J. L., Raeder, K., Collins, N., Tilmes, S., Francis, G., Clerbaux, C., Emmons,
769 L. K., Pfister, G. G., Coheur, P.-F., and Hurtmans, D.: Assessing the impacts of
770 assimilating IASI and MOPITT CO retrievals using CESM-CAM-chem and DART,
771 Journal of Geophysical Research: Atmospheres, 120, 10,501-10,529,
772 <https://doi.org/10.1002/2015JD023467>, 2015.
- 773 Bloomer, B. J., Vinnikov, K. Y., and Dickerson, R. R.: Changes in seasonal and diurnal cycles of
774 ozone and temperature in the eastern U.S., Atmospheric Environment, 44, 2543–2551,
775 <https://doi.org/10.1016/j.atmosenv.2010.04.031>, 2010.
- 776 Butler, T. J., Vermeylen, F. M., Rury, M., Likens, G. E., Lee, B., Bowker, G. E., and McCluney,
777 L.: Response of ozone and nitrate to stationary source NO_x emission reductions in the
778 eastern USA, Atmospheric Environment, 45, 1084–1094,
779 <https://doi.org/10.1016/j.atmosenv.2010.11.040>, 2011.
- 780 Chang, K.-L., Petropavlovskikh, I., Cooper, O. R., Schultz, M. G., and Wang, T.: Regional trend
781 analysis of surface ozone observations from monitoring networks in eastern North
782 America, Europe and East Asia, Elementa: Science of the Anthropocene, 5, 50,
783 <https://doi.org/10.1525/elementa.243>, 2017.
- 784 Cooper, O. R., Gao, R.-S., Tarasick, D., Leblanc, T., and Sweeney, C.: Long-term ozone trends
785 at rural ozone monitoring sites across the United States, 1990–2010, Journal of
786 Geophysical Research: Atmospheres, 117, <https://doi.org/10.1029/2012JD018261>, 2012.
- 787 Deeter, M. N., Edwards, D. P., Francis, G. L., Gille, J. C., Mao, D., Martínez-Alonso, S.,



- 788 Worden, H. M., Ziskin, D., and Andreae, M. O.: Radiance-based retrieval bias mitigation
789 for the MOPITT instrument: the version 8 product, *Atmospheric Measurement*
790 *Techniques*, 12, 4561–4580, <https://doi.org/10.5194/amt-12-4561-2019>, 2019.
- 791 Dennison, P. E., Brewer, S. C., Arnold, J. D., and Moritz, M. A.: Large wildfire trends in the
792 western United States, 1984–2011, *Geophysical Research Letters*, 41, 2928–2933,
793 <https://doi.org/10.1002/2014GL059576>, 2014.
- 794 Di, Q., Wang, Y., Zanobetti, A., Wang, Y., Koutrakis, P., Choirat, C., Dominici, F., and
795 Schwartz, J. D.: Air Pollution and Mortality in the Medicare Population, *New England*
796 *Journal of Medicine*, 376, 2513–2522, <https://doi.org/10.1056/NEJMoa1702747>, 2017.
- 797 Fahey, K. M., Carlton, A. G., Pye, H. O. T., Baek, J., Hutzell, W. T., Stanier, C. O., Baker, K. R.,
798 Appel, K. W., Jaoui, M., and Offenberg, J. H.: A framework for expanding aqueous
799 chemistry in the Community Multiscale Air Quality (CMAQ) model version 5.1,
800 *Geoscientific Model Development*, 10, 1587–1605, [https://doi.org/10.5194/gmd-10-](https://doi.org/10.5194/gmd-10-1587-2017)
801 [1587-2017](https://doi.org/10.5194/gmd-10-1587-2017), 2017.
- 802 Fiore, A. M., Jacob, D. J., Bey, I., Yantosca, R. M., Field, B. D., Fusco, A. C., and Wilkinson, J.
803 G.: Background ozone over the United States in summer: Origin, trend, and contribution
804 to pollution episodes, *Journal of Geophysical Research: Atmospheres*, 107, ACH 11-1-
805 ACH 11-25, <https://doi.org/10.1029/2001JD000982>, 2002.
- 806 Fleming, Z. L., Doherty, R. M., Schneidemesser, E. von, Malley, C. S., Cooper, O. R., Pinto, J.
807 P., Colette, A., Xu, X., Simpson, D., Schultz, M. G., Lefohn, A. S., Hamad, S., Moolla,
808 R., Solberg, S., and Feng, Z.: Tropospheric Ozone Assessment Report: Present-day ozone
809 distribution and trends relevant to human health, *Elem Sci Anth*, 6, 12,
810 <https://doi.org/10.1525/elementa.273>, 2018.



811 Gan, C.-M., Pleim, J., Mathur, R., Hogrefe, C., Long, C. N., Xing, J., Wong, D., Gilliam, R., and
812 Wei, C.: Assessment of long-term WRF–CMAQ simulations for understanding direct
813 aerosol effects on radiation “brightening” in the United States, *Atmospheric Chemistry
814 and Physics*, 15, 12193–12209, <https://doi.org/10.5194/acp-15-12193-2015>, 2015.

815 Gaubert, B., Arellano, A. F., Barré, J., Worden, H. M., Emmons, L. K., Tilmes, S., Buchholz, R.
816 R., Vitt, F., Raeder, K., Collins, N., Anderson, J. L., Wiedinmyer, C., Alonso, S. M.,
817 Edwards, D. P., Andreae, M. O., Hannigan, J. W., Petri, C., Strong, K., and Jones, N.:
818 Toward a chemical reanalysis in a coupled chemistry-climate model: An evaluation of
819 MOPITT CO assimilation and its impact on tropospheric composition, *Journal of
820 Geophysical Research: Atmospheres*, 121, 7310–7343,
821 <https://doi.org/10.1002/2016JD024863>, 2016.

822 Gettelman, A., Mills, M. J., Kinnison, D. E., Garcia, R. R., Smith, A. K., Marsh, D. R., Tilmes,
823 S., Vitt, F., Bardeen, C. G., McInerny, J., Liu, H.-L., Solomon, S. C., Polvani, L. M.,
824 Emmons, L. K., Lamarque, J.-F., Richter, J. H., Glanville, A. S., Bacmeister, J. T.,
825 Phillips, A. S., Neale, R. B., Simpson, I. R., DuVivier, A. K., Hodzic, A., and Randel, W.
826 J.: The Whole Atmosphere Community Climate Model Version 6 (WACCM6), *Journal
827 of Geophysical Research: Atmospheres*, 124, 12380–12403,
828 <https://doi.org/10.1029/2019JD030943>, 2019.

829 Hand, J. L., Schichtel, B. A., Malm, W. C., and Frank, N. H.: Spatial and Temporal Trends in
830 PM_{2.5} Organic and Elemental Carbon across the United States, *Advances in Meteorology*,
831 2013, e367674, <https://doi.org/10.1155/2013/367674>, 2013.



- 832 He, H., Liang, X.-Z., Sun, C., Tao, Z., and Tong, D. Q.: The long-term trend and production
833 sensitivity change in the US ozone pollution from observations and model simulations,
834 *Atmos. Chem. Phys.*, 20, 3191–3208, <https://doi.org/10.5194/acp-20-3191-2020>, 2020.
- 835 Im, U., Brandt, J., Geels, C., Hansen, K. M., Christensen, J. H., Andersen, M. S., Solazzo, E.,
836 Kioutsioukis, I., Alyuz, U., Balzarini, A., Baro, R., Bellasio, R., Bianconi, R., Bieser, J.,
837 Colette, A., Curci, G., Farrow, A., Flemming, J., Fraser, A., Jimenez-Guerrero, P.,
838 Kitwiroon, N., Liang, C.-K., Nopmongcol, U., Pirovano, G., Pozzoli, L., Prank, M., Rose,
839 R., Sokhi, R., Tuccella, P., Unal, A., Vivanco, M. G., West, J., Yarwood, G., Hogrefe, C.,
840 and Galmarini, S.: Assessment and economic valuation of air pollution impacts on human
841 health over Europe and the United States as calculated by a multi-model ensemble in the
842 framework of AQMEII3, *Atmospheric Chemistry and Physics*, 18, 5967–5989,
843 <https://doi.org/10.5194/acp-18-5967-2018>, 2018.
- 844 Jaffe, D. and Ray, J.: Increase in surface ozone at rural sites in the western US, *Atmospheric*
845 *Environment*, 41, 5452–5463, <https://doi.org/10.1016/j.atmosenv.2007.02.034>, 2007.
- 846 Jaffe, D., Price, H., Parrish, D., Goldstein, A., and Harris, J.: Increasing background ozone
847 during spring on the west coast of North America, *Geophysical Research Letters*, 30,
848 <https://doi.org/10.1029/2003GL017024>, 2003.
- 849 Koumoutsaris, S. and Bey, I.: Can a global model reproduce observed trends in summertime
850 surface ozone levels?, *Atmospheric Chemistry and Physics*, 12, 6983–6998,
851 <https://doi.org/10.5194/acp-12-6983-2012>, 2012.
- 852 Kumar, Rajesh, and He, C. (2023). CONUS air quality reanalysis dataset (2005-2018). Version
853 1.0. UCAR/NCAR - GDEX. <https://doi.org/10.5065/cfya-4g50>. Accessed 15 May 2024.
- 854 Kumar, R., Monache, L. D., Bresch, J., Saide, P. E., Tang, Y., Liu, Z., Silva, A. M. da,



- 855 Alessandrini, S., Pfister, G., Edwards, D., Lee, P., and Djalalova, I.: Toward Improving
856 Short-Term Predictions of Fine Particulate Matter Over the United States Via
857 Assimilation of Satellite Aerosol Optical Depth Retrievals, *Journal of Geophysical*
858 *Research: Atmospheres*, 124, 2753–2773, <https://doi.org/10.1029/2018JD029009>, 2019.
- 859 Liu, Z., Liu, Q., Lin, H.-C., Schwartz, C. S., Lee, Y.-H., and Wang, T.: Three-dimensional
860 variational assimilation of MODIS aerosol optical depth: Implementation and application
861 to a dust storm over East Asia, *Journal of Geophysical Research: Atmospheres*, 116,
862 <https://doi.org/10.1029/2011JD016159>, 2011.
- 863 Malm, W. C. and Hand, J. L.: An examination of the physical and optical properties of aerosols
864 collected in the IMPROVE program, *Atmospheric Environment*, 41, 3407–3427,
865 <https://doi.org/10.1016/j.atmosenv.2006.12.012>, 2007.
- 866 Marsh, D. R., Mills, M. J., Kinnison, D. E., Lamarque, J.-F., Calvo, N., and Polvani, L. M.:
867 Climate Change from 1850 to 2005 Simulated in CESM1(WACCM), *J. Climate*, 26,
868 7372–7391, <https://doi.org/10.1175/JCLI-D-12-00558.1>, 2013.
- 869 McClure, C. D. and Jaffe, D.: US particulate matter air quality improves except in wildfire-prone
870 areas, *PNAS*, 115, 7901–7906, <https://doi.org/10.1073/pnas.1804353115>, 2018.
- 871 Nolte, C. G., Appel, K. W., Kelly, J. T., Bhave, P. V., Fahey, K. M., Collett, J. L. J., Zhang, L.,
872 and Young, J. O.: Evaluation of the Community Multiscale Air Quality (CMAQ) model
873 v5.0 against size-resolved measurements of inorganic particle composition across sites in
874 North America, *Geoscientific Model Development*, 8, 2877–2892,
875 <https://doi.org/10.5194/gmd-8-2877-2015>, 2015.
- 876 Orozco, D., Reeves, U., and Levine, N.: Polluted Parks: How Air Pollution and Climate Change
877 Continue to Harm America’s National Parks., *National Parks Conservation Association*



878 (NPCA). Washington, DC., 2024.

879 Pagowski, M., Liu, Z., Grell, G. A., Hu, M., Lin, H.-C., and Schwartz, C. S.: Implementation of
880 aerosol assimilation in Gridpoint Statistical Interpolation (v. 3.2) and WRF-Chem (v.
881 3.4.1), *Geoscientific Model Development*, 7, 1621–1627, [https://doi.org/10.5194/gmd-7-](https://doi.org/10.5194/gmd-7-1621-2014)
882 1621-2014, 2014.

883 Parrish, D. D., Dunlea, E. J., Atlas, E. L., Schauffler, S., Donnelly, S., Stroud, V., Goldstein, A.
884 H., Millet, D. B., McKay, M., Jaffe, D., Price, H. U., Hess, P. G., Flocke, F., and Roberts,
885 J. M.: Changes in the photochemical environment of the temperate North Pacific
886 troposphere in response to increased Asian emissions, *Journal of Geophysical Research:*
887 *Atmospheres*, 109, <https://doi.org/10.1029/2004JD004978>, 2004.

888 Parrish, D. D., Millet, D. B., and Goldstein, A. H.: Increasing ozone in marine boundary layer
889 inflow at the west coasts of North America and Europe, *Atmospheric Chemistry and*
890 *Physics*, 9, 1303–1323, <https://doi.org/10.5194/acp-9-1303-2009>, 2009.

891 Pozzoli, L., Janssens-Maenhout, G., Diehl, T., Bey, I., Schultz, M. G., Feichter, J., Vignati, E.,
892 and Dentener, F.: Re-analysis of tropospheric sulfate aerosol and ozone for the period
893 1980–2005 using the aerosol-chemistry-climate model ECHAM5-HAMMOZ,
894 *Atmospheric Chemistry and Physics*, 11, 9563–9594, [https://doi.org/10.5194/acp-11-](https://doi.org/10.5194/acp-11-9563-2011)
895 9563-2011, 2011.

896 Remer, L. A., Kaufman, Y. J., Tanré, D., Mattoo, S., Chu, D. A., Martins, J. V., Li, R.-R.,
897 Ichoku, C., Levy, R. C., Kleidman, R. G., Eck, T. F., Vermote, E., and Holben, B. N.:
898 The MODIS Aerosol Algorithm, Products, and Validation, *J. Atmos. Sci.*, 62, 947–973,
899 <https://doi.org/10.1175/JAS3385.1>, 2005.

900 Saide, P. E., Carmichael, G. R., Liu, Z., Schwartz, C. S., Lin, H. C., da Silva, A. M., and Hyer,



901 E.: Aerosol optical depth assimilation for a size-resolved sectional model: impacts of
902 observationally constrained, multi-wavelength and fine mode retrievals on regional scale
903 analyses and forecasts, *Atmospheric Chemistry and Physics*, 13, 10425–10444,
904 <https://doi.org/10.5194/acp-13-10425-2013>, 2013.

905 Seyedali Mousavinezhad, Masoud Ghahremanloo, Yunsoo Choi, Arman Pouyaei, Nima
906 Khorshidian, Bavand Sadeghi, Surface ozone trends and related mortality across the
907 climate regions of the contiguous United States during the most recent climate period,
908 1991–2020,

909 Simon, H., Reff, A., Wells, B., Xing, J., and Frank, N.: Ozone Trends Across the United States
910 over a Period of Decreasing NO_x and VOC Emissions, *Environ. Sci. Technol.*, 49, 186–
911 195, <https://doi.org/10.1021/es504514z>, 2015.

912 Strode, S. A., Rodriguez, J. M., Logan, J. A., Cooper, O. R., Witte, J. C., Lamsal, L. N., Damon,
913 M., Van Aartsen, B., Steenrod, S. D., and Strahan, S. E.: Trends and variability in surface
914 ozone over the United States, *Journal of Geophysical Research: Atmospheres*, 120, 9020–
915 9042, <https://doi.org/10.1002/2014JD022784>, 2015.

916 WHO: Billions of people still breathe unhealthy air: new WHO data:
917 [https://www.who.int/news/item/04-04-2022-billions-of-people-still-breathe-unhealthy-](https://www.who.int/news/item/04-04-2022-billions-of-people-still-breathe-unhealthy-air-new-who-data)
918 [air-new-who-data](https://www.who.int/news/item/04-04-2022-billions-of-people-still-breathe-unhealthy-air-new-who-data), last access: 12 May 2024, 2023.

919 WHO: <https://www.who.int/westernpacific/health-topics/air-pollution> , last access: 12 May
920 2024, 2020.

921 Wiedinmyer, C., Kimura, Y., McDonald-Buller, E. C., Emmons, L. K., Buchholz, R. R., Tang,
922 W., Seto, K., Joseph, M. B., Barsanti, K. C., Carlton, A. G., and Yokelson, R.: The Fire
923 Inventory from NCAR version 2.5: an updated global fire emissions model for climate



924 and chemistry applications, EGU sphere, 1–45, [https://doi.org/10.5194/egusphere-2023-](https://doi.org/10.5194/egusphere-2023-124)
925 124, 2023.

926 Xing, J., Mathur, R., Pleim, J., Hogrefe, C., Gan, C.-M., Wong, D. C., Wei, C., Gilliam, R., and
927 Pouliot, G.: Observations and modeling of air quality trends over 1990–2010 across the
928 Northern Hemisphere: China, the United States and Europe, *Atmospheric Chemistry and*
929 *Physics*, 15, 2723–2747, <https://doi.org/10.5194/acp-15-2723-2015>, 2015.

930 Zhang, Y., West, J. J., Mathur, R., Xing, J., Hogrefe, C., Roselle, S. J., Bash, J. O., Pleim, J. E.,
931 Gan, C.-M., and Wong, D. C.: Long-term trends in the ambient PM_{2.5}- and O₃-related
932 mortality burdens in the United States under emission reductions from 1990 to 2010,
933 *Atmospheric Chemistry and Physics*, 18, 15003–15016, [https://doi.org/10.5194/acp-18-](https://doi.org/10.5194/acp-18-15003-2018)
934 15003-2018, 2018.